7

PAHs as a tracer for star formation

To be submitted :
E. Peeters, H.W.W. Spoon & A.G.G.M. Tielens
ASTROPHYSICAL JOURNAL, 2003

INFRARED emission features at 3.3, 6.2, 7.7, 8.6 and 11.3 μm are generally attributed to infrared fluorescense from FUV pumped large Polycyclic Aromatic Hydrocarbon (PAH) molecules. As such, these features trace the FUV stellar flux and are thus a measure of star formation. We have examined the infrared spectral characteristics of a sample of Galactic regions of massive star formation and of a sample of normal and starburst galaxies, as well as AGNs and ULIRGs. The goal of this study is to analyze various tracers of star formation with the aim of identifying the dominant processes contributing to the infrared emission from ULIRGs. We have developed a MIR/FIR diagnostic diagram based upon a Galactic sample of star forming regions. This diagnostic is derived from the far-infrared normalized 6.2 μm PAH flux and the far-infrared normalized 6.2 μm continuum flux. Within this diagram, the Galactic sources form a sequence spanning a range of 3 orders of magnitude in these ratios, ranging from embedded compact H II regions to exposed Photo Dissociation Regions (PDRs). However, the 6.2 μm PAH line-to-continuum ratio is remarkably constant over this range. We have compared our extragalactic sample to these Galactic sources. This revealed an excellent resemblance of normal and starburst galaxies with exposed PDRs. While Seyfert-2's coincide with the starburst trend, Seyfert-1's are displaced by a factor 10 in 6.2 μm continuum flux, in accordance with general unification schemes for AGNs. ULIRGs show a diverse spectral appearance. Some show a typical AGN hot dust continuum. More, however, are either starburst-like or show signs of strong dust obscuration in the nucleus. One characteristic of the ULIRGs also seems to be the presence of more prominent far-infrared emission than either starburst galaxies or AGNs. We discuss the observed variation in the Galactic sample in view of the evolutionary state and the PAH/dust abundance. Finally, we have examined the use of PAHs as quantitative tracers of star formation activity. Based on these investigations we find that PAHs may be better suited as a tracer of B stars, which dominate the Galactic stellar energy budget, than as a tracer of massive star formation.

7.1 Introduction

The mid-infrared (MIR) spectra of many objects with associated dust and gas are dominated by the well-known emission features at 3.3, 6.2, 7.7, 8.6 and 11.2 μm commonly called the unidentified infrared (UIR) bands (cf. Gillett et al. 1973; Geballe et al. 1985; Cohen et al. 1986; Roche et al. 1989). These bands are now generally attributed to vibrational emission of Polycyclic Aromatic Hydrocarbons (PAHs) containing $\simeq$ 50 carbon atoms (Léger & Puget 1984; Allamandola et al. 1985, 1989b; Puget & Léger 1989; Tielens et al. 2000). One key aspect of these IR emission features is that they are particularly bright in regions illuminated by UV bright, early type stars ($<$B1) responsible for H II regions and reflection nebulae.

With the launch of the Infrared Space Observatory (ISO), a huge amount of infrared spectral data became available, showing the omnipresent nature of these PAH features. By now, the features have been detected in a wide range of objects and environments, from post-AGB stars and planetary nebulae, to H II regions, reflection nebulae, the diffuse interstellar medium and extragalactic sources, the most distant of which is the Ultra-Luminous Infrared Galaxy (ULIRG) IRAS 03538–6432 at a redshift of z=0.3. Various studies of Galactic sources with bright PAH emission features have been performed (see e.g. the ISO special issue, A&A, 315 1996). Of particular importance here are the studies of the PAHs in a sample of H II regions, which characterized the IR emission features (and the variations among these features) in massive star forming regions (Verstraete et al. 1996; Hony et al. 2001; Peeters et al. 2002a; Vermeij et al. 2002; Verstraete et al. 2001; van Diedenhoven et al. 2003).

The MIR extragalactic ISO studies were dominated by four major programs, which focussed on the spectral properties of active galaxies (e.g. Mirabel et al. 1998; Charmandaris et al. 1999), Seyfert galaxies (e.g. Clavel et al. 2000), normal galaxies (e.g. Helou et al. 2000) and ULIRGs (e.g. Genzel et al. 1998; Lutz et al. 1998; Rigopoulou et al. 1999; Tran et al. 2001). These studies established that PAH emission features in extragalactic environments are very similar to those in Galactic star forming regions. This property has since been used qualitatively and quantitatively as diagnostics for the ultimate physical processes powering Galactic nuclei.

In an impressive study involving ISO–PHT–S and ISO–SWS observations of some 45 Active Galactic Nuclei (AGNs), starburst galaxies and ULIRGs, Genzel et al. (1998) found that the 7.7 μm PAH feature-to-continuum ratio is on average an order of magnitude smaller for AGNs than for starburst galaxies. Conversely, the ratio of the high- to low-excitation emission lines [O IV]/[Ne II] was found to be two orders of magnitude higher for AGNs than for starburst galaxies. The 7.7 μm PAH feature-to-continuum ratio was then used together with the gas excitation line ratio to separate AGNs and starburst galaxies in a 2-dimensional diagnostic plot. ULIRGs were found to reside in between the two groups, although closer to the starburst galaxies. This led Genzel et al. (1998) to conclude that 80% of the ULIRGs are predominantly powered by star formation.

A second MIR diagnostic plot was devised by Laurent et al. (2000) for the interpretation of ISO–CAM–CVF spectra of the nuclei and disks of nearby active and inactive galaxies. The diagnostic diagram separates H II regions, PDRs and AGNs on the basis of their distinctly different ratio of warm (15 μm) to hot (6 μm) continuum and the value of their 6.2 μm PAH feature-to-continuum ratio. It thereby allows to estimate the contribution of the AGN, PDRs and H II regions to a given MIR spectrum.

Clavel et al. (2000) compared the MIR spectral properties of a sample of 28 type-1 and 29

type-2 Seyfert galaxies to test AGN unification schemes. The study established that the 7.7 μm PAH luminosity distributions of both samples are the same, indicating that the properties of the Seyfert host galaxies are unrelated to the type-1/2 classification of the nuclear activity. The study also found that the average 7.7 μm PAH equivalent width of the Seyfert-1 sample is a factor $\sim$8 smaller than of the Seyfert-2 sample, implying that, on average, the 7.7 μm continuum of type-2 Seyferts is a factor $\sim$8 weaker than of type-1 Seyferts. Clavel et al. (2000) attribute this difference to dust obscuration in the nuclear environment, which, in line with the unified models for AGNs (Antonucci 1993), is attributed to the orientation of the AGN torus. An important result from this work is that except for the emission line spectrum, the 3–12 μm spectra of type-2 Seyferts appear very similar to those of normal and starburst galaxies.

The goal of this Chapter is to establish the characteristics of PAH emission bands in regions of massive star formation in the Milky Way, in order to use them as a tool for studying star formation on a galaxy-wide scale and to apply these tools to a study of extragalactic starbursts in Seyferts, (ultra-luminous) infrared galaxies and QSOs.

This Chapter is organized as follows. In Sect. 7.2, we present the observations of the MIR emission features in a sample of H II regions and ISM positions in our Galaxy, as well as in a large sample of normal, starburst, Seyfert and (ultra-luminous) infrared galaxies and QSOs. Spectral characteristics of these samples are discussed in Sect. 7.3. In Sect. 7.4, we investigate three infrared diagnostic tools designed to distinguish AGN- from starburst-dominated spectra. Sect. 7.5 highlights the PAH abundance as fraction of the total amount of dust and the application of the PAH emission bands as tracers of star formation. The conclusions are stated in Sect. 7.6.

7.2 Observations

7.2.1 H II regions and ISM

The sample of H II regions was taken from the Galactic "Ultra Compact H II region" ISO program (Peeters et al. 2002b) complemented with spectra of the Orion Bar, M17 and 30 Dor. Only those spectra with sufficient S/N are included in this sample. As a reference, we included reflection nebulae (NGC 2023, NGC 7023), heavily embedded protostars exhibiting PAH emission (MonR2 IRS2, NGC7538 IRS1), molecular clouds and the (diffuse) ISM in various regions. For details on the sources and references, see Table 7.1.

Most spectra were obtained with the Short Wavelength Spectrometer (SWS, de Graauw et al. 1996) on board the Infrared Space Observatory (ISO, Kessler et al. 1996). These spectra were taken using the AOT 01 scanning mode at various speeds with resolving power ($\lambda/\Delta\lambda$) ranging from 400 to 1500 (see Table 7.1). These data were processed with the SWS Interactive Analysis package IA^3 (de Graauw et al. 1996) using calibration files and procedures equivalent with pipeline version 10.0 or later. A detailed account of the reduction of ISO–SWS spectra can be found in Peeters et al. (2002b). Few sources were obtained with ISO–PHT–S , ISO–CAM–CVF, IRTS–MIRS and MSX with resolving power ($\lambda/\Delta\lambda$) of respectively $\sim$ 90, 35, 30 and 800. We refer to the original papers (see Table 7.1) for an account of the reduction process.

TABLE 7.1 — Journal of observations together with the derived fluxes. The coordinates of the ISO pointings are given.

Source	α(J2000)[a]	δ(J2000)[a]	Instrument[b]	TDT[c]	Ref.	6.2 PAH[d] W/m^2	cont. [5.3,5.8][d] W/m^2	cont. [6.0,.6.5][d] W/m^2	cont. [14-15][d] W/m^2	FIR[d] W/m^2	Ref. FIR
W 3A 02219+6125[♯]	02 25 44.59	+62 06 11.20	ISO-SWS 01(2)	64600609	1	2.158(-13)	3.769(-13)	4.990(-13)	4.040(-12)	1.555(-09)	1
			ISO-SWS 01(2)	78800709	1	2.363(-13)	3.375(-13)	4.874(-13)	4.384(-12)	1.555(-09)	1
30 Dor	05 38 46.00	−69 05 07.91	ISO-SWS 01(4)	17100512	2	2.606(-14)	7.179(-14)	4.839(-14)	3.084(-13)	5.915(-11)	16
OrionBar D8	05 35 18.22	−05 24 39.89	ISO-SWS 01(2)	69501409	3	3.156(-13)	2.046(-13)	3.303(-13)	1.719(-12)	-	
OrionBar BRGA	05 35 19.31	−05 24 59.90	ISO-SWS 01(2)	69502108	-	3.760(-13)	2.103(-13)	3.311(-13)	1.071(-12)	-	
OrionBar D5	05 35 19.81	−05 25 09.98	ISO-SWS 01(2)	83101507	-	5.437(-13)	2.343(-13)	3.821(-13)	1.006(-12)	3.498(-11)	17
OrionBar H2S1	05 35 20.31	−05 25 19.99	ISO-SWS 01(2)	69501806	4	3.469(-13)	1.886(-13)	3.038(-13)	6.936(-13)	-	
OrionBar D2	05 35 21.40	−05 25 40.12	ISO-SWS 01(2)	69502005	-	1.197(-13)	9.229(-14)	1.196(-13)	4.671(-13)	-	
Orion	centered on Trapezium		MSX	-	5	1.768(-5)[◇]	6.504(-06)[◇]	1.507(-5)[◇]	5.515(-05)[◇]	3.084(-3)[◇,◁]	18
IRAS 10589−6034	11 00 59.78	−60 50 27.10	ISO-SWS 01(2)	26800760	1	1.279(-13)	1.047(-13)	1.380(-13)	4.462(-13)	1.472(-10)	1
IRAS 12063−6259	12 09 01.15	−63 15 54.68	ISO-SWS 01(2)	25901414	1	1.177(-13)	1.565(-13)	1.960(-13)	5.786(-13)	1.598(-10)	1
IRAS 12073−6233[♯]	12 10 00.32	−62 49 56.50	ISO-SWS 01(2)	25901572	1	7.761(-14)	5.137(-13)	6.115(-13)	7.748(-12)	1.098(-09)	1
IRAS 12331−6134[♯]	12 36 01.9	−61 51 03.9	ISO-SWS 01(2)	29900470	1	3.565(-14)	4.316(-14)	5.469(-14)	1.524(-13)	1.336(-10)	1
IRAS 15384−5348[♯]	15 42 17.16	−53 58 31.51	ISO-SWS 01(2)	29900661	1	3.261(-13)	1.530(-13)	2.553(-13)	6.500(-13)	4.433(-10)	1
IRAS 15502−5302	15 54 05.99	−53 11 36.38	ISO-SWS 01(2)	27301117	1	9.903(-14)	2.318(-13)	2.880(-13)	9.730(-13)	8.532(-10)	1
IRAS 16128−5109[♯]	16 16 39.3	−51 16 58.3	ISO-SWS 01(2)	29402233	1	8.479(-14)	7.197(-14)	8.134(-14)	2.227(-13)	5.330(-10)	1
IRAS 17160−3707[♯]	17 19 26.1	−37 10 53.8	ISO-SWS 01(2)	32400821	1	4.369(-14)	5.544(-14)	6.819(-14)	1.453(-13)	3.508(-10)	1
IRAS 17221−3619[♯]	17 25 31.7	−36 21 53.5	ISO-SWS 01(2)	33100380	1	7.459(-14)	5.355(-14)	7.238(-14)	2.380(-13)	2.082(-10)	1
IRAS 17279−3350[♯]	17 31 18.0	−33 52 49.4	ISO-SWS 01(2)	32200877	1	9.738(-14)	5.880(-14)	8.287(-14)	2.307(-13)	1.284(-10)	1
Sgr C[♯]	17 44 35.6	−29 27 29.3	ISO-SWS 01(2)	84100301	1	6.791(-14)	3.820(-14)	2.718(-14)	2.193(-13)	-	
IRAS 17455−2800	17 48 41.5	−28 01 38.3	ISO-SWS 01(2)	28701327	1	1.147(-13)	1.238(-13)	1.809(-13)	1.033(-12)	2.286(-10)	1
IRAS 17591−2228	18 02 13.2	−22 27 58.9	ISO-SWS 01(2)	51500580	1	2.702(-14)	4.886(-14)	4.191(-14)	9.103(-14)	7.255(-11)	1
IRAS 18032−2032	18 06 13.93	−20 31 43.28	ISO-SWS 01(2)	51500478	1	1.090(-13)	7.877(-14)	1.032(-13)	3.532(-13)	3.186(-10)	1
IRAS 18116−1646	18 14 35.29	−16 45 20.99	ISO-SWS 01(2)	70300302	1	1.622(-13)	4.581(-14)	1.005(-13)	4.227(-13)	2.941(-10)	1
GGD -27 ILL[⋆]	18 19 12.00	−20 47 31.10	ISO-SWS 01(2)	14802136	1,6	1.373(-13)	2.812(-13)	2.883(-13)	5.206(-13)	2.157(-10)	1
M17 iram pos. 1	18 20 28.98	−16 11 50.78	ISO-SWS 01(2)	10201811	7	7.541(-14)	9.737(-14)	1.574(-13)	1.987(-12)	4.818(-11)	19
M17 iram pos. 2	18 20 27.59	−16 12 0.90	ISO-SWS 01(2)	09900212	7	4.477(-14)	1.443(-13)	3.046(-13)	4.069(-12)	-	
M17 iram pos. 3	18 20 26.19	−16 12 11.02	ISO-SWS 01(2)	09901413	7	1.203(-13)	1.589(-13)	2.176(-13)	3.212(-12)	-	
M17 iram pos. 4	18 20 24.79	−16 12 21.10	ISO-SWS 01(2)	09900214	7	3.345(-13)	1.588(-13)	2.494(-13)	1.279(-12)	-	
M17 iram pos. 5	18 20 23.40	−16 12 31.21	ISO-SWS 01(2)	09901415	7	2.675(-13)	1.463(-13)	2.024(-13)	4.536(-13)	-	
M17 iram pos. 6	18 20 22.09	−16 12 41.29	ISO-SWS 01(2)	09900216	7	2.033(-13)	8.342(-14)	1.505(-13)	2.258(-13)	-	
				32900866	7	2.045(-13)	1.030(-13)	1.516(-13)	1.811(-13)	-	
M17 iram pos. 7	18 20 20.70	−16 12 51.41	ISO-SWS 01(2)	09901417	7	5.807(-14)	2.105(-14)	2.979(-14)	8.304(-14)	-	
M17 iram pos. 8	18 20 19.31	−16 13 01.49	ISO-SWS 01(2)	09900218	7	5.425(-14)	5.278(-14)	6.690(-14)	1.023(-13)	1.222(-11)	19
M17 North	18 20 32.77	−16 01 42.49	ISO-SWS 01(2)	09901105	8	7.008(-14)	1.032(-13)	1.378(-13)	1.035(-13)	3.333(-11)[▷]	

TABLE 7.1 — Continued.

Source	α(J2000)[a]	δ(J2000)[a]	Instrument[b]	TDT[c]	Ref.	6.2 PAH[d] W/m^2	cont. [5.3,5.8][d] W/m^2	cont. [6.0,.6.5][d] W/m^2	cont. [14-15][d] W/m^2	FIR[d] W/m^2	Ref. FIR
IRAS 18317−0757	18 34 24.94	−07 54 47.92	ISO-SWS 01(2)	47801040	1	2.931(-13)	1.508(-13)	2.552(-13)	7.280(-13)	1.965(-10)	1
IRAS 18434−0242	18 46 04.09	−02 39 20.02	ISO-SWS 01(2)	15201383	1,6	1.881(-13)	3.583(-13)	5.111(-13)	4.410(-12)	6.982(-10)	1
IRAS 18469−0132	18 49 33.0	−01 29 03.70	ISO-SWS 01(2)	71100888	1	7.630(-14)	6.592(-14)	6.779(-14)	2.113(-13)	1.264(-10)	1
IRAS 18479−0005	18 50 30.8	−00 01 59.40	ISO-SWS 01(2)	15201791	1	3.047(-14)	9.965(-14)	9.470(-14)	5.812(-13)	2.789(-10)	1
IRAS 18502+0051	18 52 50.21	+00 55 27.59	ISO-SWS 01(2)	15201645	1	1.079(-13)	9.129(-14)	8.660(-14)	5.912(-13)	1.246(-10)	1
IRAS 19207+1410♯	19 23 02.4	+14 16 40.60	ISO-SWS 01(2)	15001041	1	6.054(-14)	6.216(-14)	5.119(-14)	2.946(-13)	3.787(-10)	1
IRAS 19442+2427⋆?	19 46 20.09	+24 35 29.40	ISO-SWS 01(2)	15000444	1,6	2.541(-13)	2.455(-13)	2.978(-13)	6.236(-13)	2.714(-10)	1
IRAS 19598+3324⋆	20 01 45.6	+33 32 43.70	ISO-SWS 01(4)	38402466	1	1.409(-13)	2.217(-12)	2.319(-12)	7.533(-12)	8.889(-10)	1
IRAS 21190+5140	21 20 44.89	+51 53 26.99	ISO-SWS 01(2)	15901853	1	9.377(-14)	9.056(-14)	1.104(-13)	8.919(-13)	8.656(-11)	1
IRAS 22308+5812	22 32 45.95	+58 28 21.00	ISO-SWS 01(2)	17701258	1,6	1.141(-13)	8.177(-14)	1.119(-13)	1.632(-13)	7.392(-11)	1
				56101082	1	1.305(-13)	8.033(-14)	1.174(-13)	1.222(-13)	7.392(-11)	1
IRAS 23030+5958	23 05 10.60	+60 14 40.99	ISO-SWS 01(2)	22000961	1	7.792(-14)	7.590(-14)	8.539(-14)	2.090(-13)	1.248(-10)	1
IRAS 23133+6050	23 15 31.39	+61 07 08.00	ISO-SWS 01(2)	22001506	1	2.454(-13)	1.369(-13)	2.129(-13)	4.924(-13)	1.959(-10)	1
NGC 7023 I♯	21 01 31.90	+68 10 22.12	ISO-SWS 01(4)	20700801	9	1.577(-13)	9.610(-14)	8.508(-14)	3.721(-14)	2.54(-12)	20
NGC 2023♯	05 41 38.29	−02 16 32.59	ISO-SWS 01(2)	65602309	10	8.275(-14)	5.643(-14)	4.665(-14)	2.431(-14)	3.04(-12)	21
NGC7538 IRS1	23 13 45.27	+61 28 09.98	ISO-SWS 01(3)	38501842	11	2.168(-13)	4.005(-12)	4.062(-12)	5.978(-12)	8.60(-10)	22
MONR2 IRS2	06 07 45.79	−06 22 50.02	ISO-SWS 01(1)	71102004	-	4.818(-13)	2.772(-12)	2.598(-12)	1.967(-12)	-	
						W/m^2/sr	W/m^2/sr	W/m^2/sr	W/m^2/sr	W/m^2/sr	
Rho-Oph	16 25 41.09	−24 06 46.90	ISO-CAM 04	09202119	12	3.738(-07)	1.150(-07)	3.975(-07)	1.659(-07)	8.931(-06)	12
SMC B1 # 1 cloud	00 45 32.50	−73 18 16.30	ISO-CAM 04	23200127	13	2.294(-08)	7.543(-09)	6.504(-09)	1.183(-09)	<0.460(-06)	13
				68602088							
Milky Way - ISM (average)			ISO-PHOT-S	-	14	3.722(-07)	2.166(-12)	2.613(-07)	-	32.30(-06)	13
NGC891 (average within 144″ from center)			ISO-PHOT-S	-	14	3.722(-07)	2.166(-12)	2.613(-07)	-	13.00(-06)	14
DISM 1	$44^\circ \leq l \leq 44^\circ 40'$, $-0^\circ 40' \leq b \leq 0^\circ$		IRTS	-	15	1.307(-07)	1.514(-07)	2.437(-07)	-	23.00(-06)	15
DISM 2	$50^\circ \leq l \leq 53^\circ$, $1^\circ \leq b < 2^\circ$		IRTS	-	15	5.139(-08)	8.234(-08)	1.350(-07)	-	10.00(-06)	15
DISM 3	$51^\circ \leq l \leq 54^\circ$, $2^\circ \leq b \leq 3^\circ$		IRTS	-	15	1.998(-08)	1.901(-08)	4.813(-08)	-	6.500(-06)	15

[a] : Units of α are hours, minutes, and seconds, and units of δ are degrees, arc minutes, and arc seconds. [b] : SWS observing mode used (see de Graauw et al. 1996). Numbers in brackets correspond to the scanning speed. [c] : each ISO observation is given a unique TDT (Target Dedicated Time) number. [d] See text for details ⋆ : water ice absorption (6 μm) present (Peeters et al. 2002a). ♯ : MIR/FIR ratio influenced by beam effects, confusion with other sources or mispointings (Peeters et al. 2002a; Martín-Hernández et al. 2003). ◇ : in units of W/m^2/sr. ◁ The contribution of IRC2 and BN is estimated on 3(4)L$_\odot$ and subtracted from the observed FIR luminosity. ▷ : obtained by integrating the LWS spectrum after scaling the LWS 45 μm flux to the SWS 45 μm flux.
References : 1 : Peeters et al. (2002b); 2 : Sturm et al. (2000) 3 : Cesarsky et al. (2000); 4 : Verstraete et al. (2001); 5 : Simpson et al. (1998); 6 : Roelfsema et al. (1996); 7 : Verstraete et al. (1996); 8 : Henning et al. (1998); 9 : Moutou et al. (1999a); 10 : Moutou et al. (1999b); 11 : Gerakines et al. (1999); 12 : Boulanger et al. (1996) 13 : Kahanpää et al. (2003); 14 : Reach et al. (2000); 15 : Onaka et al. (1996); 16 : Vermeij et al. (2002); 17 : Werner et al. (1976); 18 : Thronson et al. (1984); 19 : Meixner et al. (1992); 20 : Casey (1991); 21 : Steiman-Cameron et al. (1997); 22 : Thronson & Harper (1979)

7.2.2 ISO galaxy sample

The MIR galaxy spectra presented in this Chapter have been drawn from our database of some 250 ISO galaxy spectra, described in Chapter 2. The sample comprises normal galaxies, starburst galaxies, Seyfert galaxies, QSOs, LIRGs, ULIRGs and HyLIRGs. Depending on the size of the aperture used and the distance to the source, the spectra probe physical sizes ranging between 73 pc (4.5″) for the nearest source (Cen A; D=3.5 Mpc) and the entire disk (assuming R_{disk}=10 kpc) for galaxies beyond 170 Mpc. The MIR spectra are supplemented with infrared photometry from the IRAS Faint Source Catalog (FSC). Given a beam size of $\sim$60″, the physical sizes probed by IRAS range between 1 kpc for the nearest source and the entire disk for galaxies beyond Arp 220 (73 Mpc). For details on the data reduction of the sample, see Chapter 2.

7.3 The spectral characteristics

7.3.1 H II regions and ISM

Fig. 7.1 (middle panels) shows the MIR spectra of a few H II regions, carefully selected to span the range from highly embedded H II regions (e.g. W3) to optically visible H II regions (e.g. Orion). These IR spectra of H II regions are characterized by a strong rising dust continuum due to thermal dust emission, corresponding to dust temperatures of $\sim$ 60–70 K. Many H II regions also show strong continuum emission at $\lambda < 12\,\mu$m, whose origin is unclear. Possibly, this continuum is due to a small fraction of dust inside the H II region, heated to high temperatures by resonantly scattered Lyman-α radiation. Alternatively, these are larger ($\sim$ 500 C-atoms) PAH-like structures stochastically heated by a single or multi-photon event. On top of the dust continuum, there is a series of fine-structure lines and hydrogen recombination lines. In addition, these spectra exhibit prominent PAH emission features, often silicate absorption and in some cases absorption bands due to molecular ice species (CO_2, H_2O).

In contrast, reflection nebulae exhibit a much weaker dust continuum indicating lower dust temperatures, strong PAH emission and no fine-structure lines or recombination lines (bottom panel, Fig. 7.1). A peculiar spectrum is that of the heavily obscured H II region K3–50A, showing all characteristics of H II regions except for the dust continuum which is more similar to that of massive protostars (top panel, Fig. 7.1). This source also exhibits a multitude of ice absorption features (Peeters et al. 2002b).

Each of these emission/absorption components, characteristic for H II regions, is influenced by the local physical conditions and hence, although their global characteristics are very similar, the individual spectra display great diversity in their spectral properties (for this sample, see Roelfsema et al. 1996; Verstraete et al. 1996, 2001; Hony et al. 2001; Peeters et al. 2002a,b; Martín-Hernández et al. 2002; Vermeij et al. 2002; van Diedenhoven et al. 2003). Indeed, large variations are present in the relative strength of the PAH emission bands and the dust continuum at various wavelengths (see Fig. 7.1). While the PAH features are relatively weak in the spectra presented in the top panels (dominated by very strong dust continua), the opposite is true for the spectra in the lower panels. More specific, there seems to be a smooth trend among the H II regions in the ratio of PAH over dust continuum, ultimately evolving towards the ratio found for reflection nebulae. However, the strength of the thermal emission of dust below 20 μm is highly influenced by the dust temperature. Indeed, when normalized on the far-infrared (FIR) flux (Fig. 7.1 : right y-axis), the sequence of sources going from low to high relative strength of PAH over dust continuum is different, but, here as

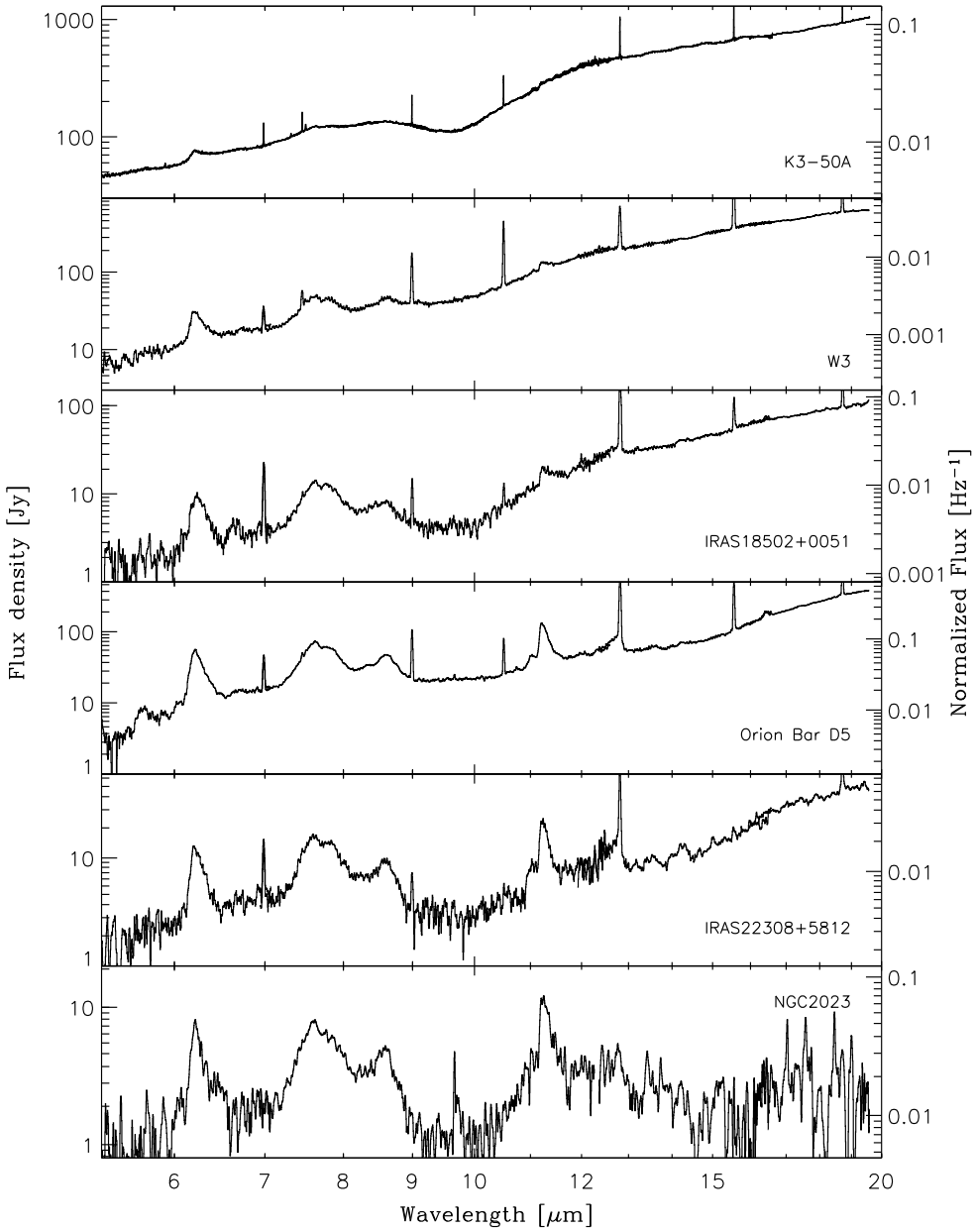

FIGURE 7.1 — Spectral variation in the mid-IR characteristics of H II regions. As a reference, the reflection nebula NGC 2023 is shown in the **bottom panel**. Note that the units on the left vertical axis represent the FIR normalized flux. Full 2–200 μm spectra for the compact H II regions can be found in Peeters et al. (2002b).

well, evolving toward reflection nebulae. This sequence indicates the evolution from highly embedded ultra-compact H II regions (e.g. W3) toward extended optically visible H II regions (e.g. Orion) and ultimately toward reflection nebulae (e.g. NGC 7023).

Similarly, the ratio of PAH over hot continuum (e.g. around ~ 6 μm) changes, albeit over a much smaller range. The latter ratio can be influenced by the possible presence of a broad emission plateau underneath the 6.2, 7.7 and 8.6 μm PAH bands of variable strength, sometimes rivalling the strength of the dust continuum at this wavelength. The beginning of this emission plateau seems to be variable, starting longwards of ~ 6 μm and extending up to ~ 9 μm.

The profile and position of the PAH emission bands in H II regions, reflection nebulae and the ISM show very little variation from source to source (Peeters et al. 2002a; van Diedenhoven et al. 2003), although spatially within a source differences have been observed (Joblin et al., in prep., Bregman & Temi, in prep.). However, the relative strength of the different PAH emission bands and hence the fraction of the total PAH flux emitted in each individual band, varies significantly from source to source and spatially within a source. This is, for example, very clear when comparing the 6.2/11.2 PAH ratio for IRAS 18502 and the Orion Bar. For a detailed discussion concerning these intensity variations, we refer to e.g. Verstraete et al. (1996), Joblin et al. (2000), Hony et al. (2001) and Peeters et al. (2002a).

Clearly, the detailed spectral characteristics of H II regions varies and hence no "typical" spectrum for H II regions exists when considering relative strengths of different emission/absorption components. Since this is partly due to the inclusion of emission of the surrounding Photo Dissociation Region (PDR) and molecular cloud in the aperture, many authors (e.g. Laurent et al. 2000; Sturm et al. 2000) have considered the spectrum of starforming regions where continuum emission at 15 μm is dominant (e.g. M 17), as the typical MIR spectrum for the H II region itself, and a reflection nebula (e.g. NGC 7023) as the typical MIR spectrum of a PDR. Indeed, the PDRs associated with compact H II regions, such as Orion, dominate the PAH emission from the region as a whole (Chrysostomou et al. 1992; Giard et al. 1992, 1994; Graham et al. 1993; Sellgren et al. 1990; Tielens et al. 1993). The spectra of H II regions (PAHs plus continuum) measured within a large beam (like that of ISO–SWS and ISO–PHT–S) are then considered to be a combination of these two typical spectra. However, as discussed above, some highly embedded H II regions have a distinct dust continuum and therefore are not taken into account in this decomposition. Sect. 7.4 discusses in detail to which extent this decomposition is valid.

7.3.2 Galaxy sample

The MIR spectra of normal and starburst galaxies reveal the same spectral features that constitute the spectra of Galactic star forming regions. Invariably, the 6–12 μm range is dominated by the family of PAH emission features at 6.2, 7.7, 8.6 and 11.2 μm (see Figure 7.2). Beyond 9 μm, starburst galaxy spectra show the additional presence of a warm dust continuum, which is weak or absent in the spectra of normal galaxies. As for Galactic H II regions, high resolution spectra also reveal many strong emission lines.

The detailed characteristics of the IR spectra depend on the properties of the galaxy in a way which is not completely understood. In particular, some starburst galaxies also show evidence for the presence of dust in the nuclear region. The nuclear spectrum of NGC 4945 (top-right panel of Figure 7.2) is a clear example of such an environment, as can be deduced

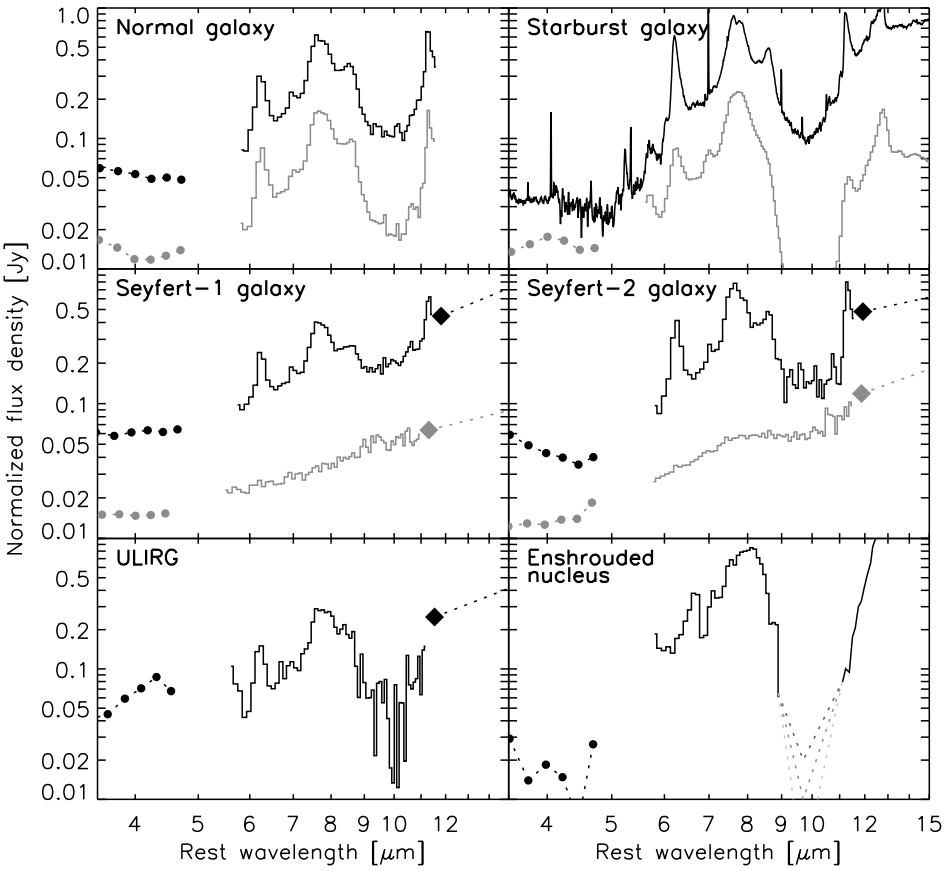

FIGURE 7.2 — MIR galaxy spectra. Dots represent ISO–PHT–SS spectroscopy rebinned to a lower resolution. IRAS 12 μm points are denoted by diamonds. **Top-left panel:** Spectra of the 'normal' galaxies NGC 4102 (*black*) and NGC 3620 (*grey*). **Top-right panel:** Spectrum of the nuclei of the starburst galaxies M 82 (*black*) and NGC 4945 (*grey*). **Mid-left panel:** Spectra of the Seyfert-1 galaxies NGC 7469 (*black*) and I Zw 1 (*grey*). **Mid-right panel:** Spectra of the Seyfert-2 galaxies NGC 5953 (*black*) and PKS 2048–57 (*grey*). **Bottom-left panel:** Spectrum of the ultra-luminous infrared galaxy UGC 5101. **Bottom-right panel:** Spectrum of the heavily obscured nucleus of NGC 4418. The spectra have been scaled by an arbitrary factor for ease of presentation.

from the weakness of the continuum and PAH features closest to the center of the 9.7 μm silicate absorption feature. The presence of a 6.0 μm water ice absorption feature further reveals that the dust is cold and stored in dense molecular clouds.

Galaxies optically classified as Seyfert galaxies contain an Active Galactic Nucleus (AGN) — a massive central black hole, surrounded by a fiercely X-ray emitting accretion disk. The disk is believed to be surrounded by a thick molecular torus, the orientation of which determines the Seyfert subtype. Galaxies optically classified as Seyfert-1 offer a direct line of sight to the accretion disk and the hot dust at the inner face of the molecular torus. For

type-2 Seyferts this direct view is blocked by the torus. In these galaxies, gas above the plane of the torus, ionized by the X-rays from the accretion disk, serves to betray the presence of the central engine. As a result of irradiation by the central X-ray source the spectra of Seyfert galaxies are characterized by emission lines from highly ionized species like Si IX, Ne V, and Ne VI, which at MIR wavelengths have lines at 3.93 μm, 14.3 & 24.3 μm and 7.65 μm, respectively (Genzel et al. 1998; Lutz et al. 2002; Sturm et al. 2002). Other than that, the MIR spectral appearance of Seyfert galaxies is quite diverse, with some spectra bearing close resemblance to those of starburst galaxies, while other spectra are dominated by a hot dust power law spectrum (see middle panels of Figure 7.2). Although the average Seyfert-1 galaxy spectrum is continuum-dominated and the average Seyfert-2 galaxy spectrum is not (Clavel et al. 2000), our ISO spectral library contains many examples of Seyfert galaxy spectra showing the properties of the converse subtype (see middle panels of Figure 7.2). Evidently, the overall MIR spectral appearance cannot be just the result of the orientation of the AGN torus, but likely also depends on the properties of the host galaxy (i.e. inclination, degree of starburst activity) as well as the power of the central engine. The spatial scale of the observations is another factor determining the MIR spectral appearance of AGNs. Observations of nearby PAH dominated Seyfert-2 galaxies, like Circinus and Cen A, have shown the spectrum of the inner 70–150 pc to be dramatically different from the spectrum of the entire galaxy, revealing an underlying, silicate-absorbed, hot dust continuum, likely associated with the central engine (Laurent et al. 2000).

A very different type of MIR spectrum is detected towards the nucleus of the luminous infrared galaxy NGC 4418 (lower-right panel of Figure 7.2). The spectrum is characterized by a prominent broad peak, centered at 8 μm, too wide and too far displaced to be attributed to 7.7 μm PAH emission. Instead, the spectrum appears to be the result of the absorption of a featureless continuum by ices and silicates, both shortward and longward of 8 μm, reminiscent of the spectrum of a deeply embedded protostar (Chapter 5). MIR imaging has further revealed the source of the absorbed MIR continuum to be extremely compact ($<$80 pc; Evans et al. 2003) and to be responsible for most of the infrared luminosity of this galaxy. In the absence of any spectral line information, the nature of the nuclear energy source is unclear and may either be extremely dense star formation or AGN activity or a combination of both (e.g. Chapter 5, Evans et al. 2003). The spectrum of NGC 4418 is not unique. Several other galaxies have been found with spectra similar to NGC 4418, most of them are ULIRGs (see Chapter 2).

The MIR spectra of ULIRGs are more complicated than the spectra of other galaxy types due to the presence of copious amounts of dust in their nuclear regions, leading to spectral distortions and strong radiative transfer effects. Figure 7.3 shows a representative compilation of available ULIRG and HyLIRG spectra, sorted by infrared luminosity. While most low-luminosity ULIRG spectra are dominated by PAH emission features, the spectra at the high-luminosity end bear close resemblance to AGN hot dust continua, showing little or no sign of PAH emission features. At intermediate luminosities some ULIRG spectra are PAH dominated, while others show signs of the presence of an NGC 4418-like broad 8 μm peak, indicating the presence of deeply enshrouded power sources. Some of these ULIRGs also show absorptions of water ice in addition (Chapter 2). A fairly typical, PAH dominated, ULIRG spectrum is further displayed in the lower-left panel of Figure 7.2.

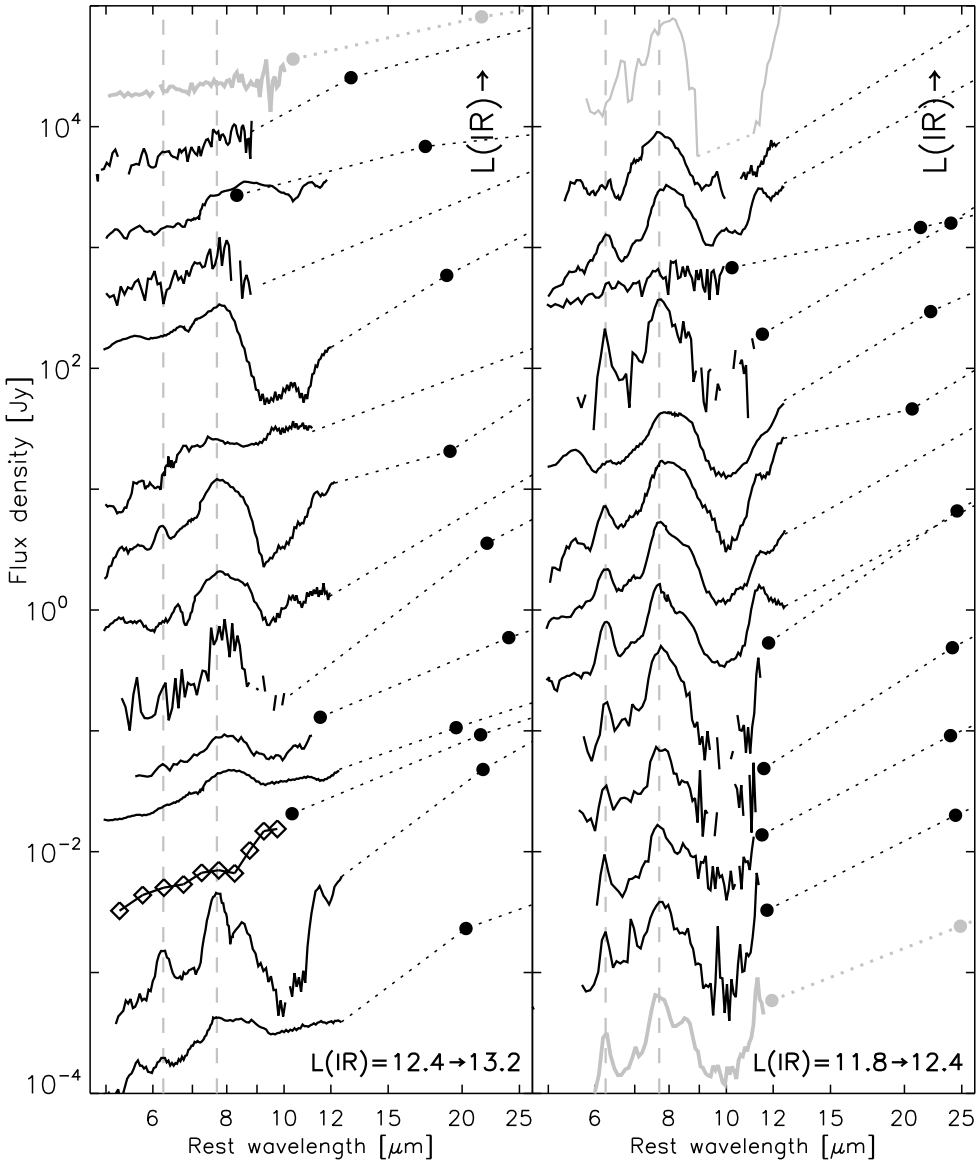

FIGURE 7.3 — ULIRG and HyLIRG spectra sorted by increasing infrared luminosity. *Vertical lines* indicate the central wavelengths of the 6.2 μm and 7.7 μm PAH features. The spectra shown in *grey* serve as template spectra for AGNs (**top-left**), starbursts (**bottom-right**) and deeply enshrouded nuclei (**top-left**). The spectra in the **left panel** are, from top to bottom: 3C 273, 15307+3252, 09104+4109, 00397–1312, 00183–7111, 23529–2119, 03538–6432, 23515-2917, 03158+4227, Mrk 231, 00275–2859, Mrk 1014, 03521+0028 and 22192–3211. In the **right panel**: NGC 4418, 17463+5806, 03000–2719, 23060+0505, 17208–0014, 00188–0856, 04384–4848, 02113–2937, 18030+0705, Arp 220, Mrk 273, 23128–5919, NGC 6240 and NGC 7552.

7.4 Diagnostic tools to distinguish AGNs and starburts

As AGNs and star forming regions have distinct spectral characteristics, their relative contribution to observed IR spectra can be determined in various ways. In this section, we focus on three different diagnostic tools, all based on the strength of PAH emission bands.

7.4.1 A MIR/FIR diagnostic

Indicative of regions predominantly powered by star formation are the strong PAH emission bands. As a measure of the strength of these PAH emission bands, we prefer the 6.2 μm band over other PAH bands, because of several reasons: 1) unlike the 3.3, 11.2 and 12.7 μm bands this band could be observed by all three MIR spectrometers onboard ISO; 2) the band is situated well outside the silicate absorption band; 3) of all major PAH emission bands, this band is the least influenced by extinction and 4) unlike the 7.7 μm feature, the band cannot be confused with a NGC 4418-like absorbed-continuum peak (see Chapters 2 and 5).

A clear line of sight towards AGN-heated hot dust may be recognized spectroscopically by the presence of a strong 6.2 μm continuum associated with a hot dust power law spectrum. Since hot dust predominantly radiates at MIR wavelengths, the ratio of 6.2 μm continuum over FIR flux will be high; far higher than for both star forming regions and AGNs without a clear line of sight to the AGN-heated hot dust. We therefore normalize our star formation indicator and our AGN hot dust indicator on the FIR flux of the source and plot these two quantities (refered to as 6.2PAH/FIR and 6.2cont/FIR) in a diagnostic diagram. A clear disadvantage of this diagnostic is the often different apertures of the MIR and FIR instruments.

For Galactic sources the strength of the hot continuum is estimated by drawing a polynomial of order 2 through points at $\sim$5.9 and $\sim$6.6 μm and integrating the flux underneath it in the range from 6.0 to 6.5 μm. Integrating the flux above this polynomial over the same range gives the strength of the 6.2 μm PAH feature. For galaxies, the continuum is determined from a linear interpolation between the fluxes at 5.9 and 6.55 μm. Other than that, the method to measure the strength of the hot continuum and the 6.2 μm PAH flux is identical to the method for the Galactic spectra. If a source exhibit water ice absorption (indicated in Table 7.1 for Galactic sources and in Chapter 2 for the galaxies), for Galactic sources a local spline continuum is determined along the wing of the water ice band to estimate the 6.2 μm PAH flux. For these sources, the 6 μm continuum strength is estimated by integrating a spline fixed right outside the ice absorption features so that the continuum strength is corrected for the ice extinction. For extragalactic sources, the 6.2 μm PAH flux is recovered by defining a continuum at the base of the 6.2 μm PAH feature and integrating the flux above it in the range of 6.0–6.5 μm. The spectra of some galaxies show no evidence for 6.2 μm PAH emission. For these galaxies upper limits for the 6.2 μm PAH flux are obtained by integrating a Gaussian with a peak flux of three times the rms noise and a FWHM of 0.185 μm. Their FIR fluxes are computed from the 60 μm and 100 μm IRAS Faint Source Catalog (FSC) fluxes, using the formula derived by Sanders & Mirabel (1996). For the compact H II regions, the FIR flux is derived by fitting a modified blackbody to the IRAS PSC fluxes (Peeters et al. 2002b). The IRAS PSC fluxes nicely correspond to the flux seen by ISO in the IRAS bands at 60 and 100 μm (Peeters et al. 2002b). However, the SWS and IRAS instruments have very different beams (20$''$ versus 90$''$). This may seriously affect the derived ratio of the MIR/FIR ratios if the source shows structure on a scale larger than the SWS beam. It probably affects about half our H II region observations. It is possible to scale the observed LWS flux to the SWS

flux at 45 μm. We opt to not apply this scaling and use the FIR as derived from the IRAS PSC fluxes, since scaling is no guarantee that the flux ratio is correct. Indeed, the dust temperature may typically vary by some 25% and the total IR flux scales with $\sim T^5$. The only exception to this is the extended molecular cloud M17–North where we did scale the LWS to the SWS observations at 45 μm. For a few sources — Orion, NGC 2023, NGC 7023, M17–SW and the ISM lines-of-sight —, higher spatial resolution data (e.g. KAO with a beam of 35–60″) exist and we have used those in our analysis (Table 7.1). Those sources, for which the MIR/FIR ratio may have been affected by spatial resolution issues are identified in Fig. 7.4 (by grey dots) and in Table 7.1. We note that these sources tend to be systematically displaced towards lower MIR/FIR ratios than the rest of the H II region sample by about a factor $\preceq$3. The derived fluxes for the Galactic sample and the extragalactic sample are given in, respectively, Table 7.1 and Spoon et al. (in prep.).

H II *regions and ISM*

As discussed in Sect. 7.3.1, both indicators vary clearly within our sample of H II regions and this range extends up to the reflection nebulae and the diffuse ISM lines of sight. This is also seen in Fig. 7.4; most sources are well localized in this diagram and are positioned along a strip going from the lower left towards the upper right, further referred to as the 'main sequence'. A clear segregation is present with embedded compact H II regions situated on the lower left side of the main sequence, while the reflection nebulae and the (diffuse) ISM are on the top right side of the main sequence. In addition, situated in the middle-right are the exposed PDRs, such as M 17 (represented by the H II region M 17–1 and the molecular clouds M17–8 and M17–North) and Orion (the Orion nebula including the Orion Bar). This segregation with object type suggests that the underlying cause might be a variation in the physical/chemical properties of the PAHs going from compact H II regions to exposed PDRs and the diffuse ISM, e.g. with G_0/n_e (Bakes et al. 2001a,b). Whether the segregation within our sample of H II regions is dominated by an evolutionary sequence — from ultra-compact to compact and then classical H II regions — is less clear. The 6.2PAH/FIR ratio correlates weakly with both the electron density and the size of the H II region (taken from Martín-Hernández et al. 2002; Martín-Hernández et al. 2003). In contrast, the 6.2cont/FIR does not show a clear dependence on either the electron density nor the size of the H II region. The latter also show large scatter in Fig. 7.4, where many H II regions lie above the main sequence. Likely, this reflects the contribution of hot dust inside the H II region. We note that metallicity does not seem to influence the location of these sources in this diagram. In particular, the SMC and 30 Dor — with metallicities 0.3 and 0.1 of solar — lie on opposite ends of this diagram.

To guide the eye, we have drawn lines of constant 6.2PAH/6.2cont in Fig. 7.4. This ratio is relatively constant within the our sample of H II regions, RNe and diffuse ISM lines of sight, ranging from 0.12 to 2.50 (excluding K3–50A). There seems to be, however, a systematic trend: H II regions tend to lie above the middle line while RNe and the diffuse ISM tend to lie between middle and lower lines. Four notable outlyers are the Orion Bar, IRAS 18116, IRAS 12073 and K3–50A. As noted above, the Orion Bar is located with the RNe suggesting a PDR dominated spectrum (cf. Tielens et al. 1993). IRAS 18116, on the other hand, has a 6.2PAH/6.2cont ratio similar to that of the RNe although it shows no other distinction in its properties with the H II regions in our sample. IRAS 12073 has the lowest 6.2PAH/6.2cont ratio of the H II regions due to its very strong hot dust continuum. Indeed, IRAS 12073 is also

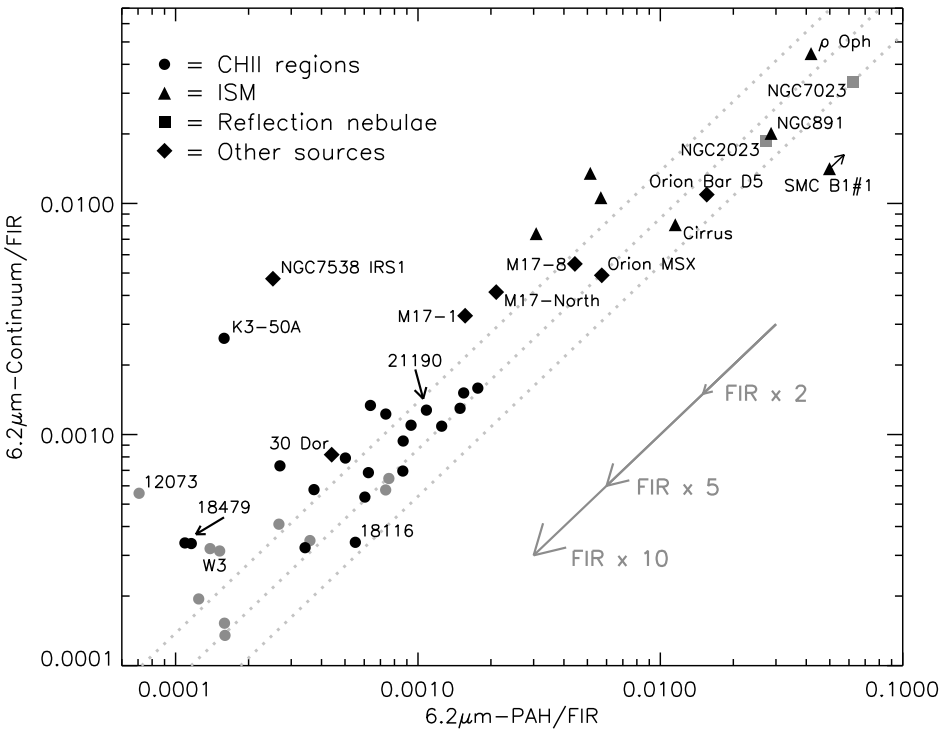

FIGURE 7.4 — A MIR/FIR diagnostic diagram. The vertical axis measures the ratio of integrated 6.0–6.5 μm continuum to FIR flux and the horizontal axis the ratio of integrated 6.2 μm-PAH to FIR flux. The three *dotted lines* are parallel to the arrows and hence correspond to a 6.2PAH/6.2cont ratio of 1.85, 1.16 and 0.72 for the lower, middle and top line, respectively. The sources possibly suffering from aperture effects are plotted in *grey*. The influence of an uncertain FIR flux is indicated by the arrows for respectively a factor of 2, 5 and 10.

the source with the largest Lyman continuum luminosity amongst the H II regions. As already pointed out, K3–50A has all the characteristics of H II regions except for its continuum which is more like that of massive protostars (see Sect. 7.3.1). The compact bipolar H II region NGC 7538 IRS1 is located close to K3–50A in this diagram.

For extended sources, the difference in aperture may influence the derived MIR to FIR ratios. In addition, the FIR beam is much larger than the MIR beam and hence confusion by nearby sources at FIR wavelengths is possible. We have indicated in Table 7.1 and Fig. 7.4 the sources suffering from these effects.

Based upon a comparison of H I recombination line fluxes and radio free-free fluxes, extinction in the MIR should be negligible for our sample of H II regions with $\tau_{\rm dust}(6.2) \leq 1$ (Martín-Hernández et al. 2002; Martín-Hernández et al. 2003). Hence, we conclude that the presence of a range in the 6.2PAH/FIR and 6.2cont/FIR ratios is real and that the sequence span by our sample likely reflects an "evolution" with object type : from embedded compact H II regions towards exposed PDRs and (diffuse) ISM.

The galaxies

As already pointed out in Sect. 7.3.2, ISO MIR spectra probe smaller physical scales than the IRAS photometers. This mismatch becomes an issue when relating MIR to FIR fluxes for nearby galaxies for which the infrared luminous regions do not completely fit within the smaller of the two apertures. We therefore have screened our sample against spectra showing clear mismatches between the IRAS 12 μm flux and the ISO 11–12 μm continuum flux. The remaining sample should therefore only consist of galaxies whose MIR emitting region fits entirely within the ISO aperture. For the IRAS-derived FIR flux we will assume that it is dominated by the same (circum)nuclear star forming regions which give rise to the MIR continuum. The final sample was subsequently created by screening the sample further against any spectrum for which the 6.0–6.5 μm continuum is so noisy that the integrated 6.2 μm flux would have to be replaced by an upper limit.

Our final galaxy sample consists of 69 AGNs (7 of which are QSO, 31 are Seyfert-1 and 31 are Seyfert-2 galaxies), 22 starburst and H II-type galaxies, 8 normal galaxies, 49 ULIRGs, 2 HyLIRGs and 3 infrared galaxies with deeply obscured nuclei (I 02530+0211, I 03344–2103 and NGC 4418). The galaxy sample is presented in Figs. 7.5, 7.6, 7.8 and 7.9.

As can be seen in the top panel of Fig. 7.5, the normal galaxies occupy a remarkably narrow strip close to the position of the exposed PDR Orion MSX. Note the extreme position of IC 860, close to 30 Dor. ISO–LWS observations have revealed this source to be very unusual in not showing any of the typical FIR fine structure lines (Malhotra et al. 2001). Also the ISO–PHT–S spectrum is not typical for normal galaxies, as it does not show 6.2 μm PAH emission. The quality of the spectrum is, however, not good enough to speculate on the nature of the MIR spectrum.

A large fraction of the starburst galaxies can be found close to the position of the normal galaxies (top panel of Fig. 7.5), with the exception of two sources, IRAS 08007–6600 and CGCG 049–057. The ISO–PHT–S spectrum of IRAS 08007–6600 (classified by Veilleux & Osterbrock (1987) as H II-type) looks very similar to AGN hot dust dominated spectra and was therefore classified by Laureijs et al. (2000) as AGN-dominated. The spectrum of CGCG 049–057, on the other hand, is PAH-dominated, but has a very strong and cold FIR continuum. Note that the starburst galaxies (excluding the two just mentioned) occupy a larger range along the ISM main sequence than the normal galaxies do, but look, on average, like exposed PDRs.

The distribution of AGNs (QSOs and Seyfert galaxies) is shown in the middle panel of Fig. 7.5. The sample seems to segregate into two groups. One group is made up mostly of Seyfert-2 galaxies with IRAS S 25/S 60 ratios all below 0.25, while the other group consists mostly of Seyfert-1 galaxies and QSOs with IRAS S 25/S 60 ratios all larger than 0.25. The galaxies in the first group all show 6.2PAH/FIR ratios in the same range as normal and starburst galaxies. In contrast, most of the galaxies in the second group only have formal 6.2PAH/FIR upper limits, some of which are found at 6.2PAH/FIR ratios 2–3 times larger than the highest value found for normal and starburst galaxies. These upper limits shift left and fit in with the rest of their group if the scaling by FIR flux is replaced by a scaling by the total infrared flux (8–1000 μm; Sanders & Mirabel 1996). Diagrams based on the IR flux are shown in Fig. 7.6. In line with the orientation dependent unification scheme (Antonucci 1993), the segregation in 6.2cont/FIR between the two groups likely reflects the orientation of the toroid structure around the nucleus which for the first (lower) group may block our line of sight to the warm inner toroid, responsible for the 6 μm continuum. Assuming this to

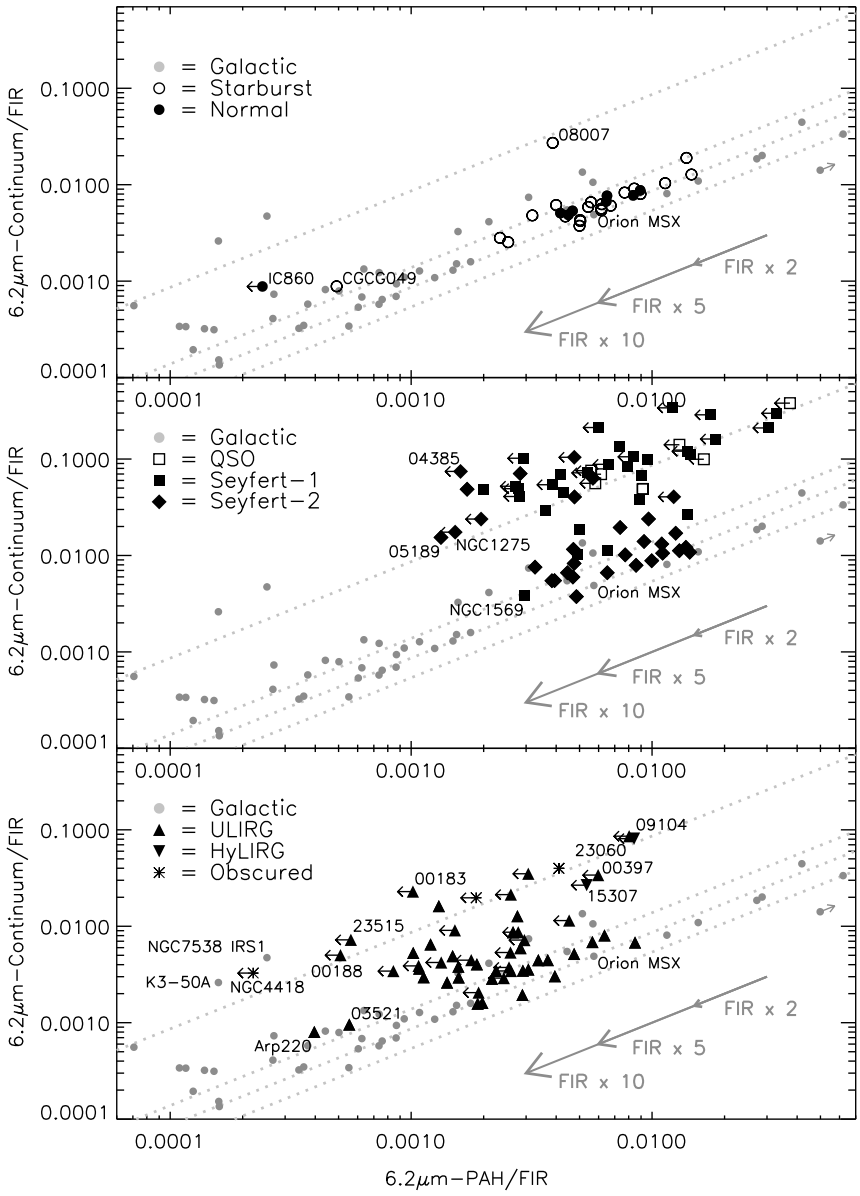

FIGURE 7.5 — MIR/FIR diagnostic diagram for different type of galaxies. The vertical axis measures the ratio of integrated 6.0–6.5 μm continuum to FIR flux and the horizontal axis the ratio of integrated 6.2 μm-PAH to FIR flux. *Grey* circles correspond to H II regions and the ISM sources. The three parallel *dotted lines* and the arrows are as in Fig. 7.4. The top *dotted line* corresponds to a 6.2PAH/6.2cont ratio of 0.12.

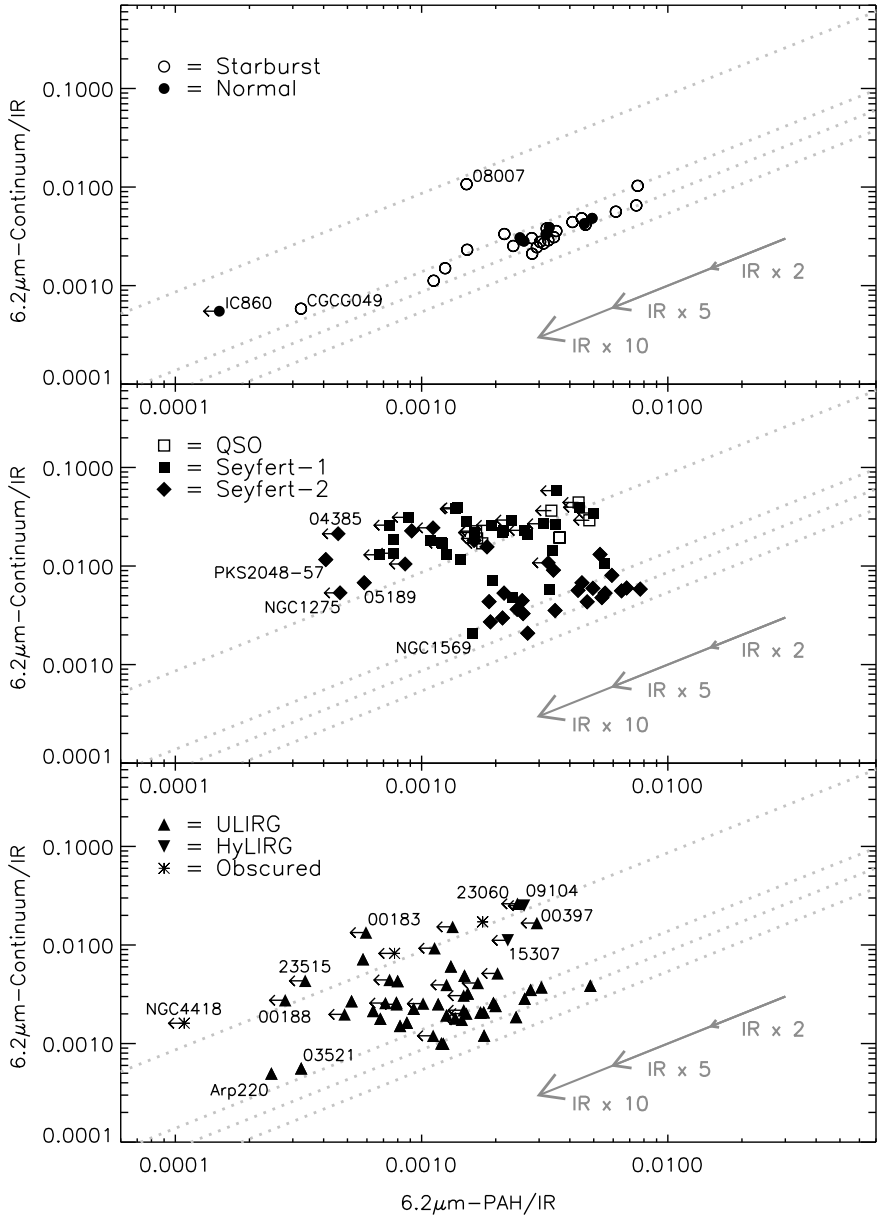

FIGURE 7.6 — MIR/IR diagnostic diagram for different type of galaxies. The vertical axis measures the ratio of integrated 6.0–6.5 μm continuum to IR flux and the horizontal axis the ratio of integrated 6.2 μm-PAH to IR flux. The three parallel *dotted lines* and the arrows are as in Fig. 7.4. The top *dotted line* corresponds to a 6.2PAH/6.2cont ratio of 0.12.

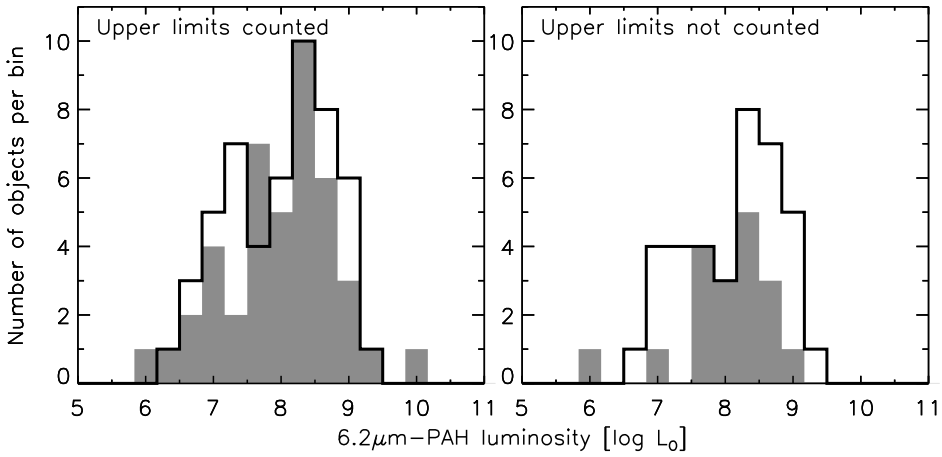

FIGURE 7.7 — Luminosity distribution of the 6.2 μm PAH feature for Seyfert-1 galaxies (*grey*) and Seyfert-2 galaxies (*black*). The bin sizes are 0.33 dex. **Left panels:** Upper limits on the PAH flux are counted as detections. **Right panels:** Upper limits on the PAH flux are excluded.

be the case, a separation of a factor 10 in 6.2cont/FIR may be interpreted as an A(V)=50–150 (depending on the choice of extinction law), which (assuming a normal gas to dust ratio N_H=1.9×10^{21} A_V) is equivalent to a column density of $10^{23.0}$–$10^{23.5}$ cm^{-2}. This range is in good agreement with the mean Seyfert-2 absorbing column, as measured directly from X-ray data (Risaliti et al. 2002), and with the results of Clavel et al. (2000). The presence of some type-1 Seyferts in the lower cloud (NGC 1569, Mrk 789 and NGC 7469) would then imply that the intrinsic power of the AGN in these galaxies must be small for the AGN hot continuum not to dominate the MIR spectral appearance. Alternatively, the AGN hot continuum and the optical AGN diagnostic lines emanating from these three galaxies are obscured by patchy foreground dust clouds along the line of sight in the host galaxy, but still allowing an optical classification. Conversely, the presence of some type-2 Seyferts in the upper cloud (NGC 1068, NGC 1275, Mrk 463, IRAS 04385–0828, NGC 5506 and PKS 2048–57), would then be explained by a direct line of sight, at grazing angle, to the inner edge of the torus, or by the presence of dust clouds above the plane of the torus, which are irradiated and heated by the central source.

One of the key predictions of the orientation dependent unification scheme is that the properties of the Seyfert host galaxies are independent of the orientation of the torus and, hence, independent of the Seyfert type. Clavel et al. (2000) have tested this by measuring the 7.7 μm PAH luminosity distributions for type-1 and type-2 Seyferts and found that they were the same. We have repeated this test for our entire sample of Seyfert galaxies (43 Seyfert-1's; 51 Seyfert-2's). The resulting luminosity distributions are shown in Figure 7.7. If upper limits are counted as detections, both Seyfert types have the same median 6.2 μm PAH luminosity of $10^{8.1}$ L$_\odot$. If upper limits are excluded, the median values are still very similar, $10^{8.2}$ L$_\odot$ for type-1 and $10^{8.3}$ L$_\odot$ for type-2 Seyferts. Our results are therefore consistent with those of Clavel et al. (2000).

Given a similar range of 6.2 μm PAH luminosities for all Seyferts, it is interesting to note that the range of 6.2cont/FIR and 6.2PAH/FIR ratios found for continuum-dominated Seyferts extends to lower values than for PAH-dominated Seyferts. These sources are therefore likely enriched in FIR flux, as opposed to deficient in 6.2 μm PAH flux. The outlyer I 05189–2524, for example, has a 6.2 μm PAH luminosity four times above average ($<$L(6.2PAH)$>$ = $10^{8.25}$ L$_{\odot}$) and I 04385–0828, at roughly the same 6.2PAH/FIR, has an average PAH luminosity. Both sources hence exhibit a FIR excess, as is likely also the case for most other Seyferts at this end of the distribution. The MIR spectrum of both sources is unusual. I 05189–2524 is the only Seyfert galaxy in our sample displaying a 6.0 μm water ice absorption, while I 04385–0828 shows a deep 9.7 μm silicate feature, which is also unusual. Further inspection of the samples of continuum-dominated and PAH-dominated AGNs reveals that the galaxies at the lower end of both distributions are not scattered along a line of constant line-to-continuum ratio, but rather along a line of constant 6.2cont/IR (Fig. 7.6), indicating a decreasing 6.2 μm PAH line-to-continuum ratio. Possibly, this indicates that the nuclei of Seyferts at the lower 6.2PAH/FIR end of the two distributions are more dusty than Seyferts at the other end of the two parallel distributions.

Even more dusty are the nuclei of most ultra-luminous infrared galaxies. The distribution of ULIRGs, HyLIRGs and galaxies with deeply obscured nuclei, is shown in the lower panel of Fig. 7.5. These objects cover a large portion of this diagram, reflecting their wide-ranging properties. Galaxies in the upper right section of the plot (e.g. I 00397–1312, I 00275–2859, I 09104+4109, I 15307+3252 and I 23060+0505), all have IRAS S 25/S 60 ratios and MIR spectra similar to AGNs in that same section. These ULIRGs and HyLIRGs are likely AGN-dominated. In contrast, some ULIRGs show spectra similar to Orion MSX and other bonafide star formation regions and are likely dominated by star formation. Many other ULIRGs occupy a space not covered by any other (extra)galactic source, roughly limited by the lower end of both Seyfert distributions, and the far-off position of the deeply enshrouded nucleus of NGC 4418. These ULIRGs are therefore likely very dusty or composite objects, made up of an NGC 4418-like embedded nucleus and circumnuclear star formation. Two notable outlyers are Arp 220 and I 03521+0028, which are found among the CH II regions, close to the position of another outlyer, IC 860. Since the spectrum of Arp 220 is deficient in emission lines (Chapter 6) — characteristic of CH II regions — this source is likely shifted down from the ULIRG domain, due to the presence of an additional strong FIR component, which is not commonly present in other ULIRGs (Chapter 6). Given their close proximity to Arp 220, I 03521+0028 and IC 860 may also harbor similar FIR bright components.

Fig. 7.8 shows the distribution of a subset of galaxies in which the 6.0 μm water ice feature has been identified (Chapter 2), the so-called 'ice galaxies'. The sample has been appended with two galaxies (I 03344–2103 and I 02530+0211), which show similarly deep silicate absorption features as the class 1 and class 2 ice galaxies. However, shortward of the silicate feature both spectra show features which are likely artefacts. For I 02530+0211 it is nevertheless clear that the 5.8–6.5 μm spectrum is feature-free. Likewise, for I 03344–2103 the presence of weak 6.2 μm PAH emission can be confirmed, the presence of a 6.0 μm water ice absorption feature, however, not.

The presence of 6.0 μm water ice absorption causes the continuum in the 6.0–6.5 μm range to be depressed with respect to its intrinsic value. The distorting effect is minor for weakly ice-absorbed sources like Mrk 231, I 05189–2524 and I 00183–7111, but substantial for sources with both a strong continuum and an appreciable ice optical depth, like I 00188–

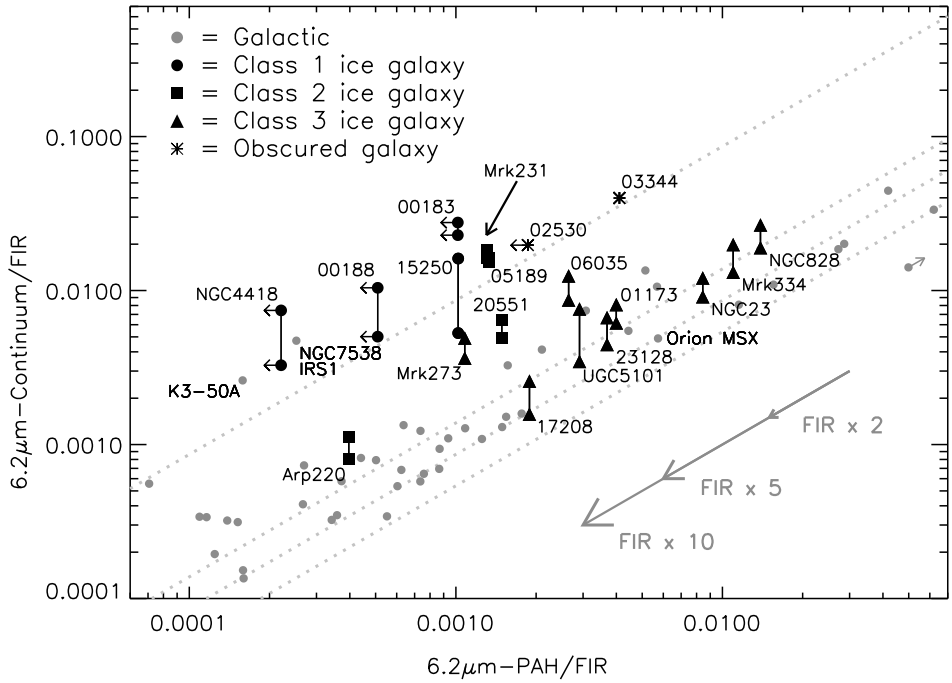

FIGURE 7.8 — MIR/FIR diagnostic diagram for deeply obscured galaxies and ice galaxies. The vertical axis measures the ratio of integrated 6.0–6.5 μm continuum to FIR flux and the horizontal axis the ratio of integrated 6.2 μm-PAH to FIR flux. The four parallel *dotted lines* and the *arrows* are as in Fig. 7.5. A vertical *black line* indicates the upward shift of an ice galaxy if the measured 6.2 μm continuum is corrected for the presence of 6.0 μm water ice absorption.

0856, NGC 4418, I 15250+3609 and UGC 5101. As can be seen in Fig. 7.8, these latter sources shift up by a factor 2–3 if the model continua derived in Chapter 2 are used as intrinsic continuum for the 6.0–6.5 μm range.

Class 3 ice galaxies, showing weak 6.0 μm ice band absorptions, coincide with the location of the normal and starburst galaxies in this diagram. Compared to class 3, class 1 ice galaxies, with no obvious PAH features and strong 6.0 μm ice and silicate bands are shifted upwards and to the left in Fig. 7.8, betraying the addition of extra MIR continuum as well as FIR continuum. The few class 2 ice galaxies, with weak PAHs and moderate ice absorptions, are more scattered throughout this plot. Some (I 20551–4250) fall in between the two other classes. Others coincide with class 1 (Mrk 231 and I 05189–2524). Arp 220, which has weak ice absorption, has shifted downwards along the Galactic trend and is an outlier in this diagram (see above). It is clear that the absorption associated with molecular clouds can influence the location of a region in this diagram. In particular, we note that the extreme example of this class, NGC 4418, has shifted all the way to in between the two extreme embedded Galactic sources associated with molecular cloud material, K3–50A and NGC 7538 IRS1.

The infrared characteristics of our sample can also be described in a mid-infrared/total-infrared (MIR/IR) diagram. Close inspection of the distribution of the various galaxy types over this diagram (Fig. 7.10) reveals that in this diagram the AGNs also segregate into an upper and a lower group; the ULIRGs seem to be a continuation of these two AGN groups towards lower MIR/IR. The slope of the two parallel distributions seems to be far shallower than the slope of the main sequence. As discussed before for the Seyfert sample in the context of the MIR/FIR diagram, we suggest that galaxies at the lower end of the two distributions may be more dusty. Indeed, the galaxies at 6.2PAH/IR$<6\times10^{-4}$ are predominantly ice galaxies.

In Chapter 2 we proposed that the classification of ice galaxy spectra may reflect an evolutionary sequence from strongly obscured beginnings of star formation (and AGN activity) to a less enshrouded stage of advanced star formation (and AGN activity). Assuming NGC 4418 to represent the earliest, most obscured stage after a galaxy collision or a galaxy merger, evolution would then proceed towards the lower distribution for galaxies which in the MIR are dominated by star formation (and may contain a Seyfert-2 nucleus), or towards the upper distribution for galaxies which in the MIR are AGN-dominated.

Application of diagnostic

MIR galaxy spectra can show the spectral characteristics of star forming regions, AGN-heated dust and/or obscuration (see Sect. 7.3.2). As pointed out above, spectra of clear lines of sight to AGN-heated dust are located in other parts of the MIR/FIR diagnostic diagram than spectra for which this line of sight is blocked by the AGN torus and which therefore are PAH-dominated. In order to better understand the connection between these two groups we have calculated the diagnostic ratios that result from adding AGN hot dust to several choices of PAH-dominated spectra. As pure AGN-heated dust template, we used the nuclear spectrum of the prototypical Seyfert-1, NGC 4151, and set its 6.2PAH/FIR ratio equal to 0. As the FIR flux associated with AGN hot dust has not been directly measured for NGC 4151 (nor for any other galaxy), we determine two values for its 6.2cont/FIR ratio, assuming 25% and 50% of the IRAS FSC flux to be associated with the AGN hot dust. As starburst template, we choose the central region of the starburst galaxy M 83. Other PAH dominated galaxy spectra along the main sequence are subsequently mimicked by scaling the FIR flux up and down by a factor 3. Dashed and dash-dotted lines in Fig. 7.9 represent the calculated mixing lines, further referred to as 'AGN-starburst' tracks. These tracks strikingly illustrate the direction in which a Seyfert galaxy spectrum would move if the obscuring dust in the line of sight to the hot inner wall of the torus would be removed. The absence of Seyfert galaxies along the horizontal (upper) part of the mixing lines may be taken as a further confirmation that AGNs in the upper group only differ from those in the lower group by an obscuration equivalent to a factor of 10–50 in 6 μm brightness.

Similarly, starburst galaxies and heavily obscured galaxies are found in far-apart regions in the MIR/FIR diagnostic diagram. We illustrate the connection between these two groups by calculating the diagnostic ratios that result from adding PAH dominated spectra to an heavily obscured spectrum. In this way, we mimick the degree of obscuration. As a template for a heavily obscured galaxy, we used the Galactic massive protostar NGC 7538 IRS1, located close to NGC 4418. We further used the same starburst templates as for the AGN-starburst tracks, but added another main sequence 'starting' point in the lower left quadrant, by scaling the FIR flux of M 83 up by a factor 30. These mixing lines — further refered to as 'obscured-

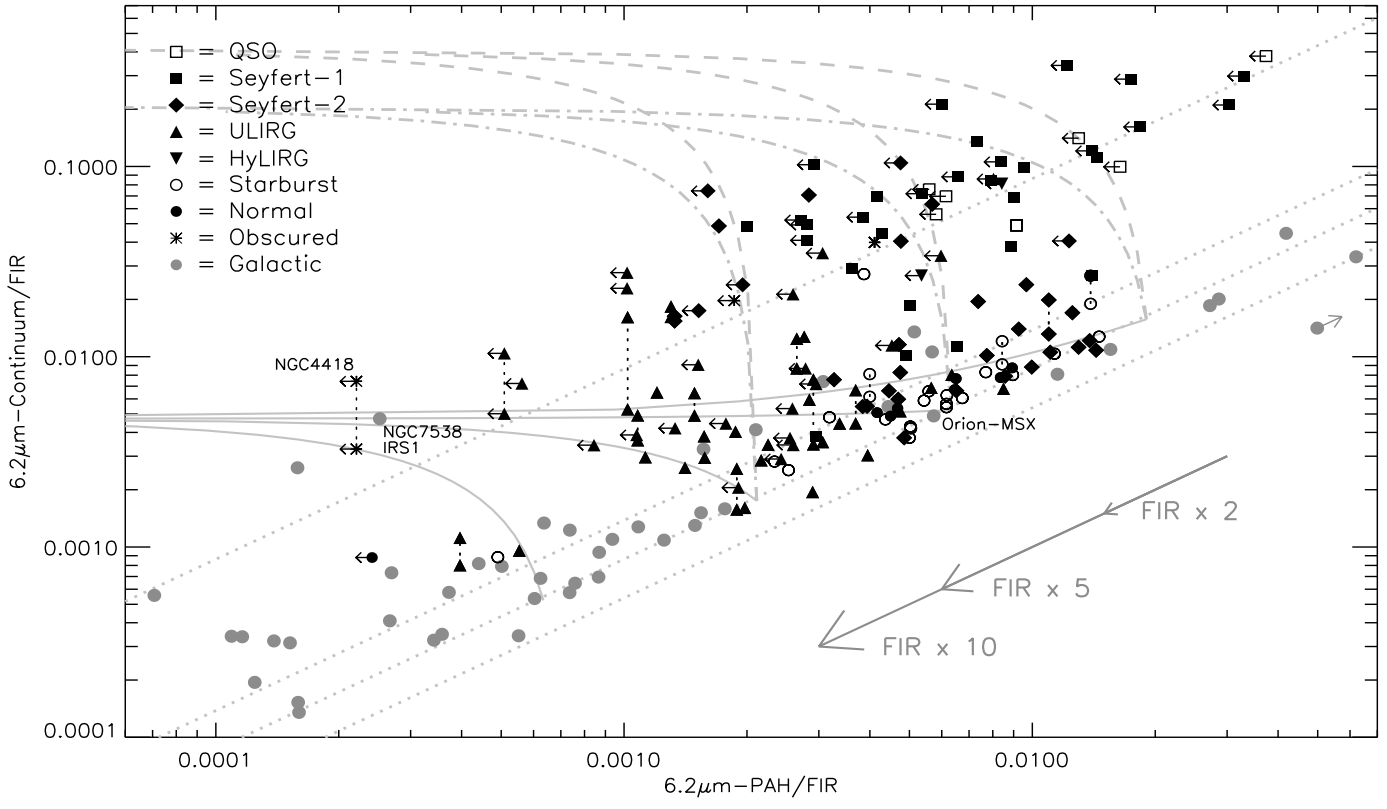

FIGURE 7.9 — The MIR/FIR diagnostic diagram for all sources. The vertical axis measures the ratio of integrated 6.0–6.5 μm continuum to FIR flux and the horizontal axis the ratio of integrated 6.2 μm-PAH to FIR flux. The *dotted lines* and the *arrows* are as in Fig. 7.5. The *continuous lines* are mixing lines between heavily obscured and exposed star formation. The mixing lines from starburst- to AGN-dominated MIR spectra are represented by the *dashed* and *dot-dashed lines*, assuming respectively 25% and 50% of the IRAS FSC flux to be associated with AGN hot dust. See text for details.

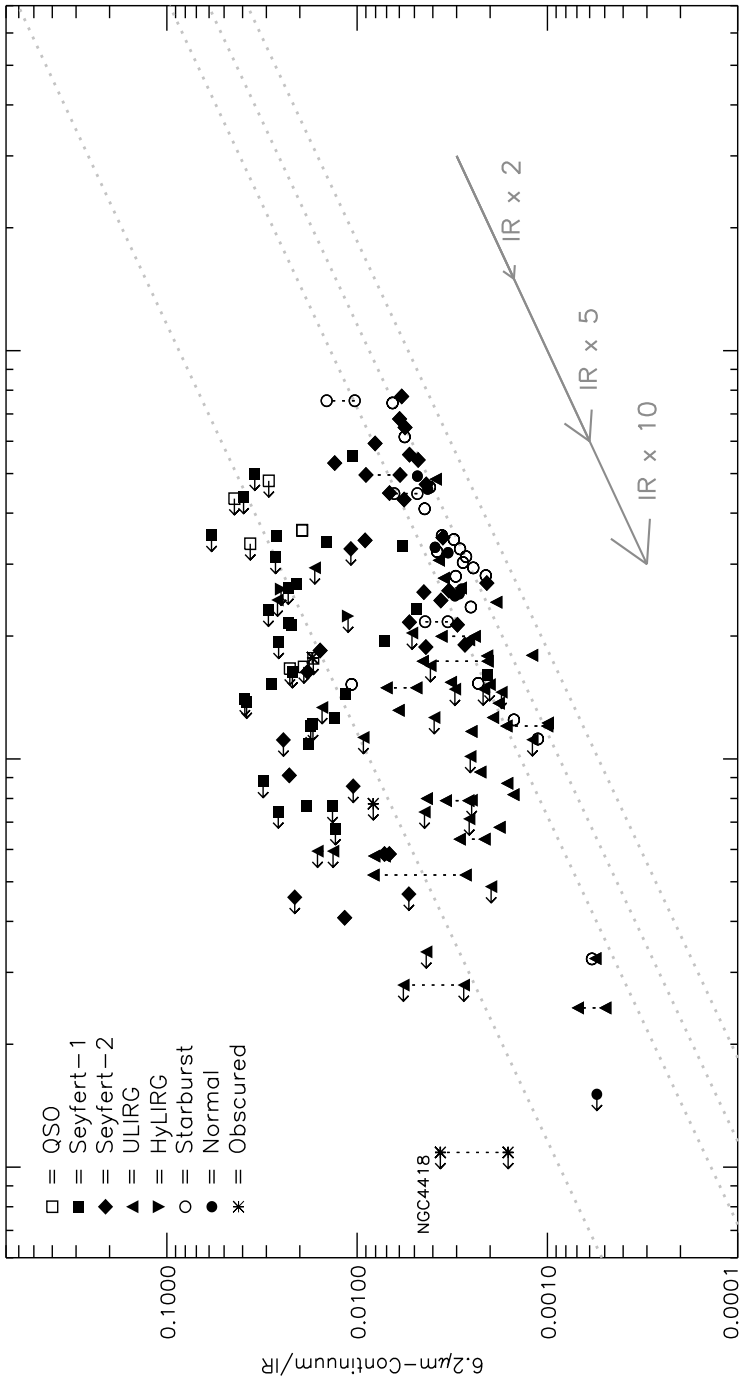

FIGURE 7.10 — MIR/IR diagnostic diagram for extragalactic sources. The vertical axis measures the ratio of integrated 6.0–6.5 μm continuum to IR flux and the horizontal axis the ratio of integrated 6.2 μm-PAH to IR flux. The dotted lines and the arrows are as in Fig. 7.5.

starburst' tracks — are shown by solid lines in Fig. 7.9. Note that H II regions located above the main sequence do not necessarily suffer from obscuration.

As can be seen in Fig. 7.9, on the main sequence no galaxies are found with 6.2PAH/FIR ratios below 0.002–0.003. Assuming this to be the lowest attainable 6.2PAH/FIR value for pure starburst *galaxies*, our tracks suggest that galaxies found at 6.2PAH/FIR$<$0.002 must contain an obscured nuclear component. Interestingly, this would then indicate that a large fraction of the ULIRG nuclei is obscured. Note that our simple mixing model does not offer an explanation for the extreme positions of Arp 220, IC 860, CGCG 049–057 and I 03521+0028, found in the lower left quadrant of the diagram.

7.4.2 Laurent diagnostic diagram

Another diagnostic solely based on the MIR spectrum has been proposed by Laurent et al. (2000). These authors assume that the MIR emission of galaxies is a composition of emission from 1) AGN-heated dust, characterised by a strong dust continuum shortwards of 10 μm, 2) PDRs, characterized by a PAH emission spectrum, and 3) H II regions, characterized by strong dust continuum longwards of 10 μm. To quantify their relative contributions, two diagnostic indicators are used, the ratio of warm (14–15 μm) to hot (5.1–6.8 μm) dust continuum and the ratio of 6.2 μm PAH emission to hot dust continuum. Note that the latter indicator is similar to the offset (6.2PAH/6.2cont) of a source from the main sequence in the MIR/FIR diagnostic.

We have chosen to sample the hot continuum at a somewhat shorter wavelength than done by Laurent et al. (2000), in order to be a) more sensitive to the slope between hot and warm continuum and b) to avoid sampling within the 6.0 μm water ice absorption band. Our prefered integration range for the hot continuum therefore runs from 5.3 to 5.8 μm. For the warm continuum we adopt the same integration range as Laurent et al. (2000): 14.0–15.0 μm. The 6.2 μm PAH flux is determined in the same way as discussed in the previous section. The derived fluxes for the Galactic sample and the extragalactic sample are given in, respectively, Table 7.1 and Spoon et al. (in prep.).

H II *regions and ISM*

The H II regions do not form a narrow sequence in this diagram but rather show a wide spread scattering over about 1/3 of the plot. However, they do avoid the low PAH to warm continuum properties of the AGNs. The Orion Bar is now positioned with the H II regions — with strong PAHs and moderately warm continuum — instead of with the reflection nebulae. Obviously, Galactic sources which are not on the main sequence in the MIR/FIR diagram (i.e. with unusual 6.2PAH/6.2cont ratios) are also outlyers in the Laurent diagram (i.e. at correspondingly unusual 6.2PAH/5.5cont ratios). In the Laurent diagram outlyers are, however, more apparent. For the rest, similar conclusion can be drawn as for the MIR/FIR diagnostics. First, metallicity seems not to influence the location of the sources in the diagram, as exemplified by the distinct locations of 30 Dor and the SMC in the diagram. Second, massive protostars (NGC7538 IRS1 and Mon R2 IRS2, but also K3–50A) are found at low 6.2PAH/5.5cont and low 15cont/5.5cont, clearly away from most other H II regions and much closer to the AGN template. Likewise, IRAS 18479, an H II region suffering from heavy extinction, is situated near the center of the diagram. Note that correcting for extinction (for sources with known A_K) does not reduce the observed spread. However, it clearly has some influence on the

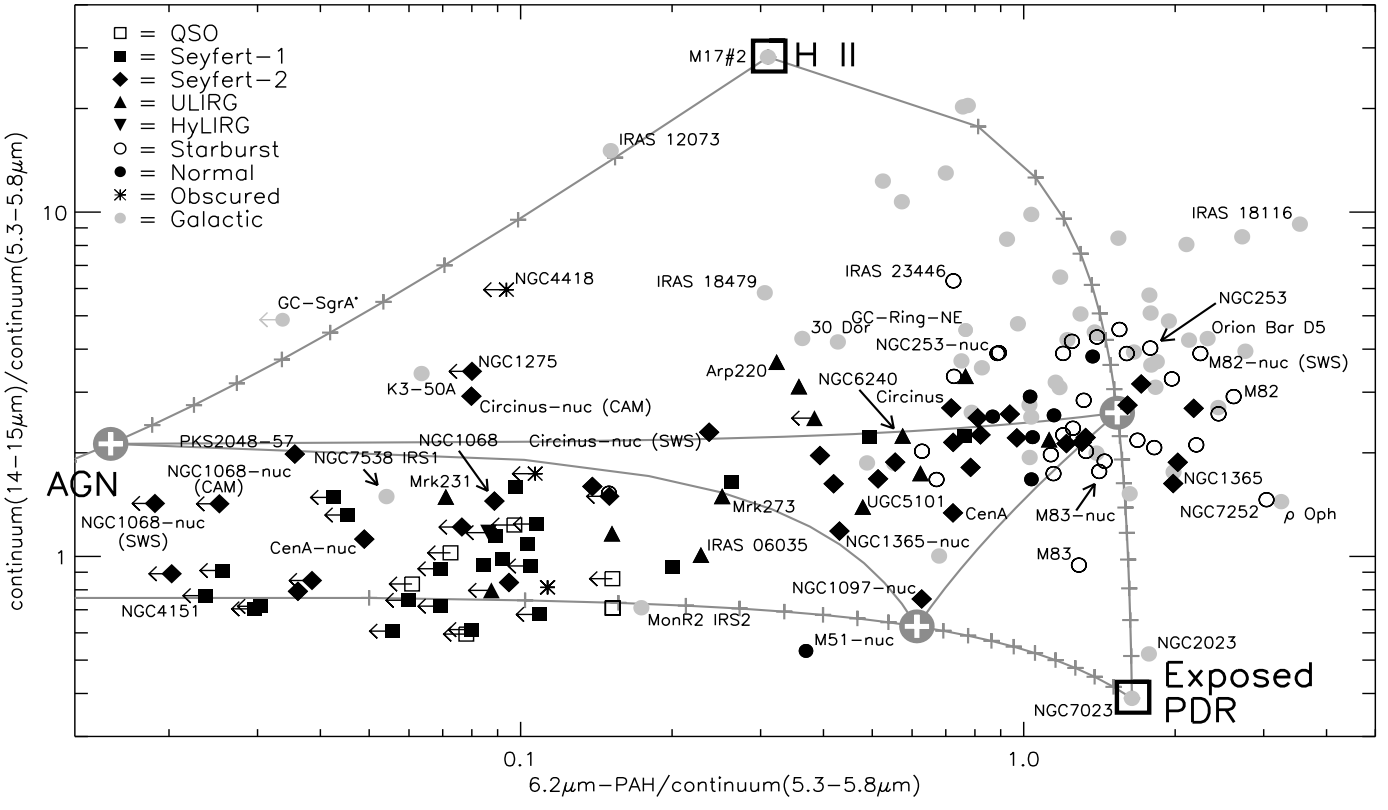

FIGURE 7.11 — MIR diagnostic diagram adapted from Laurent et al. (2000). The *grey lines* connecting the three template positions are mixing lines between the templates. Each *grey cross* indicates a 5% change in relative contribution. *Thick crosses* mark equal contribution of two templates. The *grey lines* connecting the three *thick crosses* indicate a constant 50% fraction of one component along each line. The SMC source B1#1 is located off the diagram at position (3.0,0.16).

precise position of the sources; an A_K of 2, which is typical for these H II regions (Martín-Hernández et al. 2002; Martín-Hernández et al. 2003), gives rise to an increase of 7% and 15% in 6.2PAH/5.5cont and 15cont/5.5cont, respectively.

Galaxies

The selection criteria for this diagram are somewhat different than for the 6.2PAH/FIR vs. 6.2cont/FIR diagram, as not all galaxy spectra are available over the full 5.3–15.0 μm range. ISO–PHT–S spectra, for instance, only cover the ranges 2.47–4.77 μm and 5.84–11.62 μm. For targets at low redshift this means that the 5.3–5.8 μm hot continuum spectrum cannot be measured directly. We therefore performed a linear interpolation over the 4.77–5.84 μm gap for those spectra which have sufficient S/N on either side of the gap. Targets which did not meet this criterium, mostly ULIRGs, were eliminated from the sample. Note that for sources with redshifts z>0.1 the gap in the ISO–PHT–S spectral coverage is not an issue. As mentioned above, ISO–PHT–S spectra also present a problem at the long wavelength end, as their wavelength coverage stops at 11.62 μm. In order to derive a 14–15 μm continuum for these cases, we logarithmically interpolated the IRAS 12 μm and 25 μm fluxes to the 14–15 μm range. However, sources were removed from the sample if their IRAS 12 μm fluxes are upper limits, or if there is a clear mismatch between the ISO–PHT–S spectrum and the IRAS 12 μm flux. While the former criterium results in the exclusion of many fainter ULIRG spectra (including the ULIRGs from the ZZULIRG proposal (Tran et al. 2001), whose ISO–CAM–CVF spectra do not extend beyond 13 μm), the latter criterium results in the deselection of many nearby galaxies. The final sample was created after screening against sources with 5.3–5.8 μm spectra which are either too noisy or which show artefacts, as is the case for several ISO–CAM–CVF spectra.

Our final galaxy sample consists of 66 AGN spectra (6 QSO, 23 Seyfert-1 and 37 Seyfert-2 spectra), 30 starburst and H II-type galaxy spectra, 7 normal galaxy spectra, 13 ULIRG spectra, one HyLIRG spectrum (I 09104+4109) and 3 spectra of infrared galaxies with deeply obscured nuclei (I 02530+0211, I 03344–2103 and NGC 4418). Note that some galaxies are close enough for ISO to obtain spectra of both the central region and the entire ISO–CAM–CVF field of view. These galaxies are NGC 253, NGC 1068, NGC 1365, NGC 1808, Cen A, Circinus and M 83. In Fig. 7.11 these galaxies are included with both their integrated and their nuclear spectra.

Fig. 7.11 clearly shows that the large majority of galaxy spectra is found in a wide strip, running almost horizontally across the diagram, with a few clear outlyers. This sequence runs from normal and starburst galaxies on the right (coinciding with the H II regions), through the ULIRGs in the middle (overlapping to some extent with the Galactic embedded star forming regions) to the Seyfert 1's on the left. Seyfert 2's are predominantly located on the right, but are found along the full range, depending on the degree of dilution of the AGN hot dust continuum by a PAH dominated spectrum, which depends on both the physical size covered by the aperture and the fraction of the bolometric luminosity contributed by star formation. We note especially the close similarity between the MIR characteristics of the Orion Bar and the nucleus of starburst galaxy M 82. This similarity does, however, end here, as the spectrum of the entire M 82 field-of-view tends more towards that of a reflection nebula. The same trend is observed for M 83. Apparently, galaxy disks are dominated by stellar types which give rise to reflection nebulae. At the other end of the galaxy sequence, the AGN MIR spectra show little to no discernable 6.2 μm PAH emission on top of a pure hot

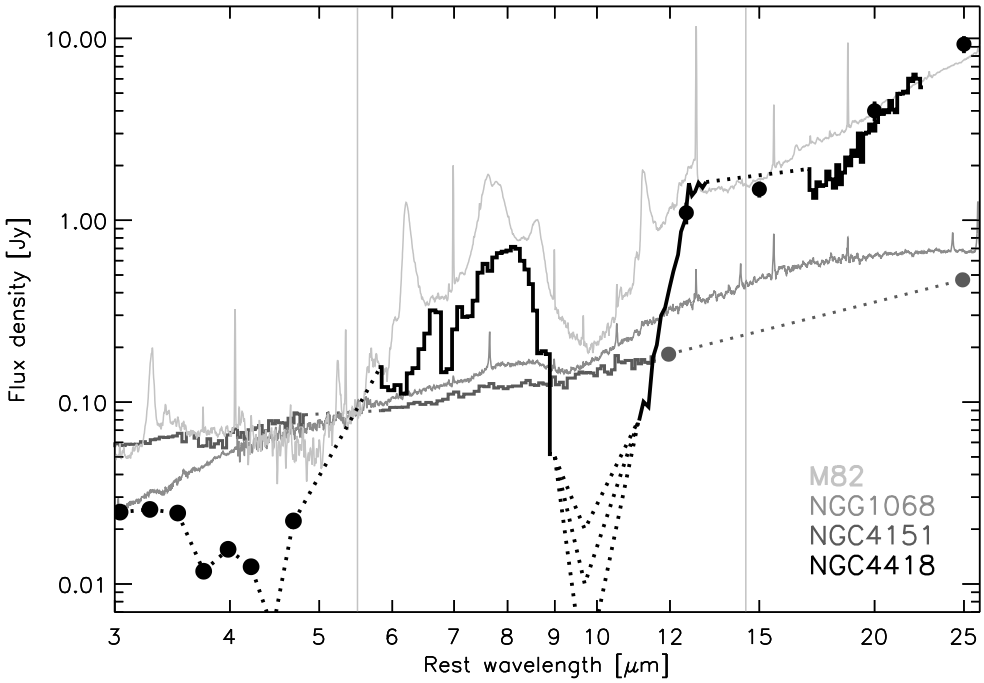

FIGURE 7.12 — Comparison of the MIR spectra of the nucleus of M 82 (*light grey*), the nucleus of NGC 1068 (*middle grey*), the nucleus of NGC 4151 (*dark grey*) and the deeply obscured nucleus of NGC 4418 (*black*). Vertical lines denote the central wavelengths of the hot (5.5 μm) and warm (14.5 μm) continuum integration ranges.

dust continuum. Fig. 7.12 reveals small differences in continuum slope among AGN nuclei, for example in the nuclear spectra of NGC 1068 (Seyfert-2) and NGC 4151 (Seyfert-1). As already pointed out by Laurent et al. (2000) on the basis of their sample of ISO–CAM–CVF spectra, the spectra of the AGN host galaxies are dramatically different from those of the AGN itself and resemble those of normal and starburst galaxies instead. A good example is the nearby Seyfert-2 galaxy Cen A (Laurent et al. 2000). While its integrated galaxy spectrum is PAH dominated and can be found among the starburst galaxies, the nuclear spectrum shows hardly any PAH emission and is situated with the AGNs.

Unlike the MIR/FIR diagram, where ULIRGs occupy their own niche, ULIRGs in the Laurent diagram are not separated out as much. Some ULIRGs (Mrk 231 and I 23060+0505) and the HyLIRG I 09104+4109 are found among the pure AGNs, while other ULIRGs, like I 17208–0014, are found among the starburst galaxies. The remaining ULIRGs are found more towards the center of the plot.

A highly obscured source, like NGC 4418, has a ratio of warm-to-hot continuum which is very similar to that of the prototypical starburst galaxy M 82. However, it lacks the strong

6.2 μm PAH feature of M 82. Conversely, its 6.2PAH/5.5cont ratio is typical of pure AGN spectra, but the slope of its continuum is much steeper. Other sources with moderate to strong obscuration include the galaxies I 02530+0211 and I 03344–2103 (indicated by asteriks in Fig. 7.11). The range over which these sources are scattered includes the domain of the pure AGNs and most of the AGN-dominated portion of the strip leading towards the position of the Orion Bar and M 82.

Note that the ULIRG Arp 220 is located in between NGC 4418 and the average position of starburst galaxies. This is in good agreement with the results of MIR spectral composition presented in Chapter 6.

Application of diagnostic

Similar to Laurent et al. (2000), we calculated mixing lines where the contribution of each template to the MIR flux (measured from 5.3 to 16 μm) varies between 0 and 100% (see Fig. 7.11). The three templates used, are the spectra of NGC 7023 (exposed PDR template), M 17 at position 2 (H II template) and NGC 4151 (AGN-heated dust template, see Fig.7.12). The templates are represented in Fig. 7.11 by large open squares. We assumed a PAH flux of zero for the AGN template instead of the formally derived upper limit. It is important to realize that the mixing percentages can only be interpreted as percentages of *mid*-infrared and not *total* infrared luminosity. This is especially true for the AGN contribution, as the same AGN may have a factor 10 higher or lower continuum flux, solely depending on the degree of obscuration towards the central source.

It is clear that our sample of H II regions is not solely dominated by emission of hot dust from the H II region but also shows a significant contribution of the surrounding PDR. However, the sequence from PDRs to H II regions is much less well determined observationally. Using other H II and PDR templates would change the position of the mixing line. Indeed, this is forcefully brought home by the many objects which lie outside the mixing lines which span the diagram. In any case, changing the templates will not remove the spread of the observed H II regions along a mixing line. Hence, H II regions can only be described in first order by a combination of an H II and PDR template.

Embedded protostars can be easily distinguished from H II regions and PDRs in this diagram by their lower 6.2PAH/5.5cont ratio. Unfortunately, however, their location coincides with that of AGN-dominated spectra. Therefore, this diagnostic diagram cannot distinguish well between MIR spectra which are AGN-dominated or dominated by a deeply embedded source. This is of particular interest to ULIRGs whose MIR spectra can have the signature of star formation, AGN-heated dust or dust extinction (Sect. 7.3.2). With this diagram, only the first can be discerned.

The PAH contribution to the MIR spectrum of Seyferts is best traced by the 6.2PAH/5.5cont ratio, which is highly sensitive to small fractions of PDR (Orion Bar) contribution included within the beam. These contributions usually arise from circumnuclear star formation rings or from the galaxy disk. Note that for starburst galaxies, which lack an active nucleus, the inclusion of a larger part of the galaxy disk does not result in a similar strong shift in either diagnostic ratio.

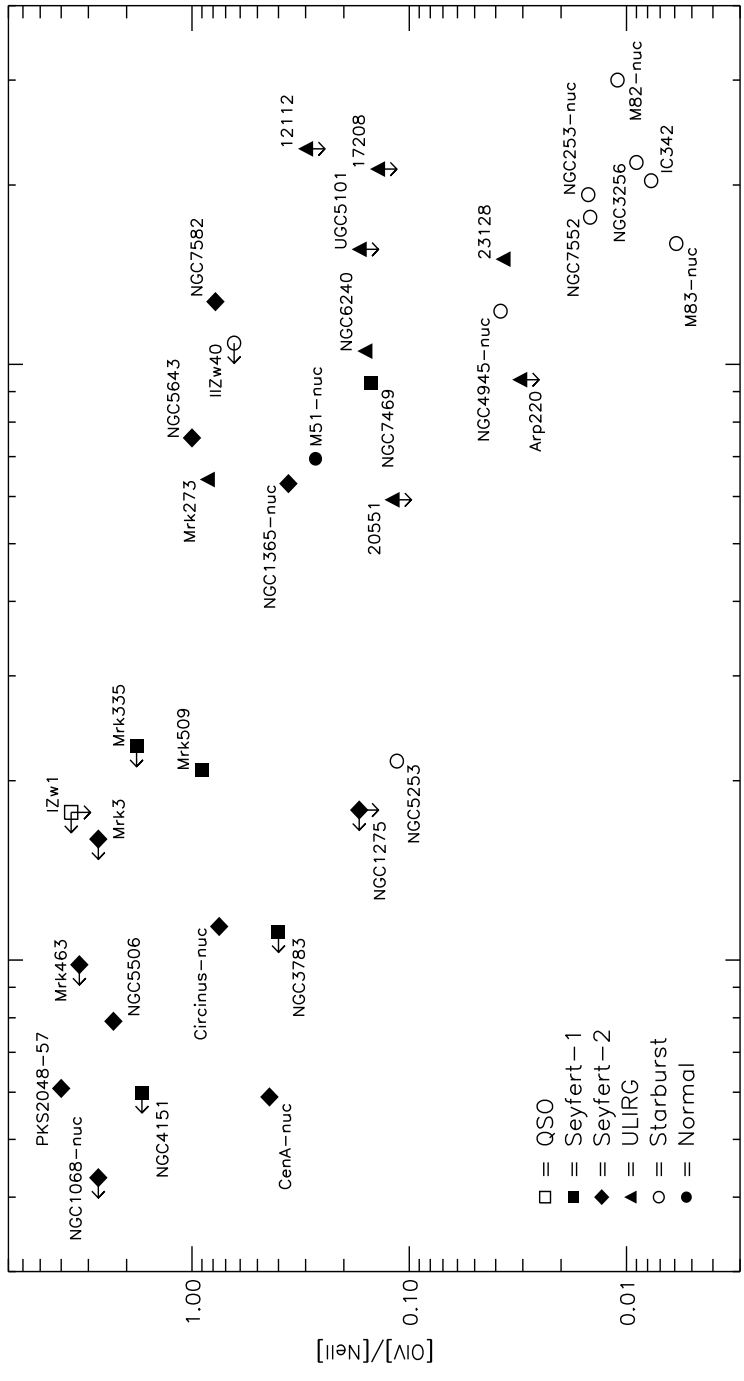

FIGURE 7.13 — MIR diagnostic diagram for different type of galaxies, adapted from Genzel et al. (1998). The vertical axis measures the ratio of 25.9 μm [O IV] (high excitation) to 12.8 μm [Ne II] (low excitation) and the horizontal axis measures the 6.2PAH/6.2cont ratio. AGN-dominated MIR spectra are found in the upper left quadrant, while starburst-dominated MIR spectra are found in the lower right quadrant.

7.4.3 The Genzel diagnostic diagram

A MIR diagnostic diagram which succesfully separates Seyfert galaxies from starburst galaxies is the diagram originally proposed by Genzel et al. (1998). Following the discussion in the previous sections, the use of the 6.2 μm PAH line-to-continuum (or equivalently the use of the 7.7 μm PAH line-to-continuum) is an excellent choice for determining the importance of star formation for the MIR flux. Indeed, while the flux varies by orders of magnitude relative to the FIR flux, their ratio is very constant in Galactic star forming regions. Conversely, the observed variation in the 6.2PAH/FIR ratios in the Galactic sample invalidates this ratio as a tracer of the contribution of star formation to the total infrared luminosity.

Here we show a modified version of this diagram, in which we replaced the 7.7 μm PAH line-to-continuum ratio by the ratio based on the 6.2 μm PAH feature (Fig. 7.13). The diagram classifies the sources as AGN- or starburst-dominated according to their position along the arc extending from fully AGN-dominated (upper left) to fully starburst-dominated (lower right).

The number of galaxies in our Genzel diagram is limited by the availability of line fluxes of 12.81 μm [Ne II] and 25.9 μm [O IV] from the literature. For AGNs the line fluxes were taken from Sturm et al. (2002), for starburst galaxies from Verma et al. (2003) and for ULIRGs from Genzel et al. (1998). Our final sample consists of 17 AGNs (1 QSO, 5 Seyfert-1, 11 Seyfert-2), 8 ULIRGs, 9 starburst galaxies and 1 normal galaxy.

Fig. 7.13 clearly illustrates that the [O IV]/[Ne II] ratio is effective in separating Seyfert from starburst galaxies, as Seyferts have ratios higher than 0.1 and starburst galaxies have ratios lower than $\sim$0.02. Note especially the Seyferts NGC 7469 and NGC 7552, which appear starburst-like in their 6.2 μm PAH line-to-continuum ratio, but which are AGN-like in their [O IV]/[Ne II] ratios.

Several of the Seyferts in the upper left quadrant of the diagram are represented by the properties of their nuclei (high excitation gas and low 6.2 μm PAH line-to-continuum ratio). Were these galaxies to be represented by their integrated-galaxy properties instead (higher 6.2 μm PAH line-to-continuum ratio and lower excitation, contributed by the starburst), these sources would move considerably to the right and also down. Circinus and Cen A, for example, would shift by more than an order of magnitude to the right, towards NGC 7469 and NGC 7582, and also down (by an unknown amount), towards the ULIRGs NGC 6240 and UGC 5101. At this position, only their high [O IV]/[Ne II] ratios would identify them as Seyferts. Applying the [O IV]/[Ne II] ratio to find AGNs in ULIRGs, only 2 out of 8 ULIRGs seem to harbour an AGN. These ULIRGs are NGC 6240 and Mrk 273. The other 6 ULIRGs either have upper limits or have a ratio intermediate to those typical for Seyferts and starbursts (e.g. I 23128–5919).

The nucleus of the nearby starburst galaxy NGC 4945 is found at an intermediate [O IV]/[Ne II] ratio. Hard X-ray observations have shown this galaxy to contain a buried AGN (Iwasawa et al. 1993; Guainazzi et al. 2000), which so far has escaped detection at NIR and MIR wavelengths. The elevated [O IV]/[Ne II] ratio for this source is likely due to strong differential extinction between 12.81 μm and 25.9 μm in this notoriously dusty nucleus (Chapter 3). However, the example of NGC 4945 may be taken as a warning that some AGNs may escape detection also from MIR excitation indicators like [O IV]/[Ne II]. Other highly obscured Galactic nuclei, like NGC 4418 and Mrk 231, have not even been detected in 12.81 μm [Ne II] (Genzel et al. 1998, Chapter 5). For these galaxies, and likely also for many ULIRGs, the Genzel diagnostic diagram is not well suited.

7.4.4 Comparison of the three diagnostic diagrams

Each of the three diagnostic diagrams is constructed with the immediate goal to reveal the identity of a galaxy.

Heavily obscured galaxies are best recognized in the MIR/FIR diagram. Since they show no fine-structure lines, they are absent in the Genzel diagram while in the Laurent diagram — which was also not constructed for these type of galaxies — they can be mistaken for AGN-dominated sources. Only the MIR/FIR diagram seems to be able to separate out ULIRGs showing signatures of obscured star formation.

The ability to identify type-1 Seyferts is possible with all three diagnostics. However, only the Genzel diagram is able to break the degeneracy between starburst and Seyfert-2's. Indeed, by using the [O IV]/[Ne II] ratio, the Seyferts are clearly separated from the starburst galaxies. In contrast, starburst galaxies and Seyfert-2's occupy the same region in the MIR/FIR and Laurent diagnostic diagram. This illustrates that the identification of the dominant power source — AGN or starburst — highly depends on the wavelength region considered. Conversely, such an identification does not imply a similar degree of dominance in the *total* infrared luminosity. Obviously, no AGN signature can be observed in the IR for a heavily obscured nucleus and hence none of the three diagrams will work.

7.5 Discussion

7.5.1 PAH abundance

The ratio of the total emission in the PAH emission bands to the FIR emission measures the competition of the PAHs and the dust for the illuminating FUV photons and is, thus, an indicator for the PAH/dust abundance. To first order, this can be measured by the 6.2PAH/FIR ratio due to the fact that the fraction of total PAH flux emitted in the 6.2 μm PAH band varies only slightly from about 14 to 38 % with an average of 28$\pm$4% (Vermeij et al. 2002; Peeters et al. 2002a). The observations presented here (Figs. 7.4 through 7.9) show variations in 6.2PAH/FIR of almost 3 orders of magnitude. Thus, the observations seem to imply that the PAH abundance in the ISM varies over three orders of magnitude. Moreover, this ratio nicely breaks up the Galactic sources according to object type (see Sect. 7.4.1). Thus, PAHs seem to be much more abundant in the diffuse ISM than in embedded or compact H II regions.

Studies of PAH/FIR ratios in Galactic sources have revealed that this ratio is independent of the local radiation field, G_0, for low radiation fields and decreases with G_0 at higher radiation fields (Boulanger et al. 1998a,b; Onaka 2000). These authors suggested that this linearity of PAH strength with G_0 for low G_0 is consistent with emission coming from species small enough to be stochastically heated. The decrease for high G_0 is then taken to indicate a decreasing abundance of these species relative to that of the grains with increasing strength of the illuminating radiation field.

The observed segregation in our sample with object type seems to support this at first sight. The sources with the lowest G_0 also have the highest 6.2PAH/FIR ratios, while the compact H II regions characterized by high G_0's have much lower 6.2PAH/FIR ratios. However, closer inspection reveals that there is no clear relationship between 6.2PAH/FIR and G_0. Fig. 7.14 shows the variation between 6.2PAH/FIR and G_0 for the sample of H II regions with G_0 varying over almost 4 orders of magnitude. Extended or complex H II regions are excluded due to possible aperture effects. Possibly, there is a very weak relationship between 6.2PAH/FIR and G_0. However, we emphasize that sources with similar 6.2PAH/FIR show a

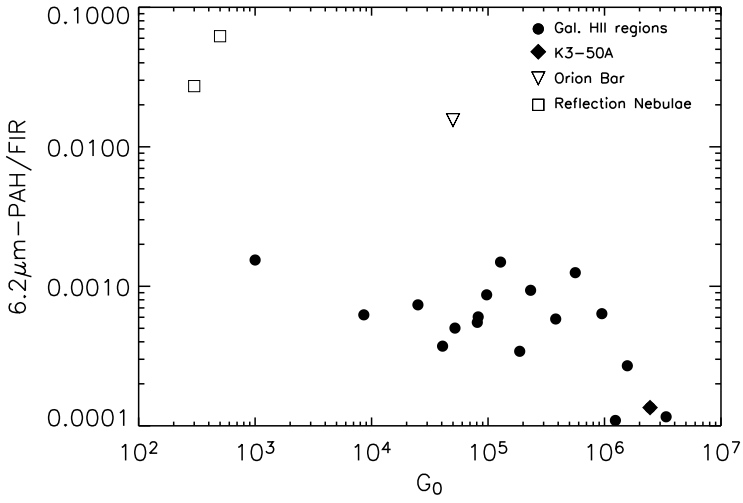

FIGURE 7.14 — The relation of 6.2PAH/FIR with the radiation field for H II regions. As a reference, two RNe are also shown in this plot.

large spread in G_0; up to a factor 130. Boulanger et al. (1998a,b) considered only 2 sources in this G_0 range; the reflection nebula NGC 7023, located in the top-left corner of Fig. 7.14, and the PDR associated with the H II region M17 with a 6.2PAH/FIR ratio similar to the ratio found in the H II regions. In our study, these two sources also show a decrease of 6.2PAH/FIR with G_0. But this trend is not confirmed in our larger sample. In contrast, Onaka (2000) found a loose correlation between 7.7PAH/FIR versus G_0 for different positions within the Carina Nebula (with only a factor up to 7 difference in G_0 for positions with similar 6.2PAH/FIR). The presence of such a relationship within a single object seems to be a more general characteristic of the PAH emission behavior. Apparently, within a single object, variations in G_0 are important in driving the emission spectrum. However, the source to source variation in the PAH/FIR ratio does not seem to follow G_0, but is rather dominated by other factors. The observed variation in the 6.2PAH/FIR demonstrates that PAHs compete much better for FUV photons in the diffuse ISM than in compact H II regions. This may reflect the destruction of PAHs inside the ionized gas volume. In particular, dust can be present inside H II regions and thereby absorb much of the FUV flux before it even reaches the surrounding PAH-rich PDRs. The importance of PAH destruction in the ionized gas will increase with decreasing size of the H II region because this corresponds to a larger dust optical depth in the ionized gas for a given dust abundance. Possibly, the observed large spread in the 6.2PAH/FIR ratio with G_0 reflects the variation in the internal dust content of H II regions. It is fair to say, however, that at this point the origin of the large variation in the 6.2PAH/FIR ratio is unclear.

7.5.2 PAHs as a tracer of star formation

Star formation properties of galaxies are essential in assessing their evolutionary histories. Different tracers for star formation are used based upon integrated colors, the UV continuum, recombination and forbidden lines and FIR emission (e.g. Kennicutt 1998, and references

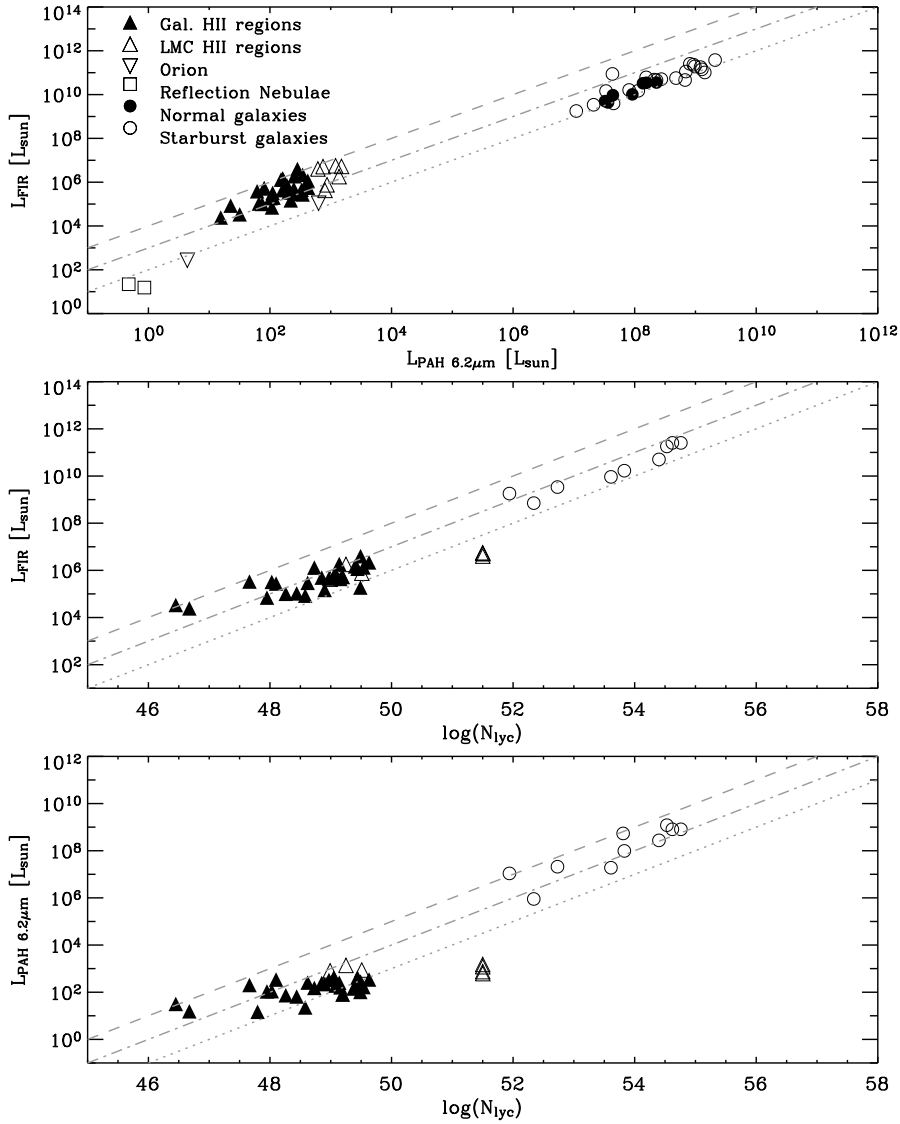

FIGURE 7.15 — Three tracers of star formation, 6.2 PAH luminosity, log (N_{lyc}) and FIR luminosity plotted against each other for a wide variety of sources; i.e. Galactic H II regions, LMC H II regions (taken from Vermeij et al. 2002) and normal and starburst galaxies. In case of a distance ambiguity for the Galactic H II regions, only the far distance is shown. The isolated group of triangles refer to 4 positions within 30 Dor. The other LMC H II regions are situated outside 30 Dor. The *grey lines* (*dotted*, *dash-dotted*, *dashed*) indicate a 6.2 PAH luminosity equal to respectively 1, 0.1 and 0.01 % of the FIR luminosity (**top panel**), a N_{lyc}/L_{FIR} ratio of respectively 10^{44}, 10^{43} and 10^{42} (**middle panel**) and a $N_{lyc}/L_{6.2PAH}$ ratio of respectively 10^{47}, 10^{46} and 10^{45} (**bottom panel**).

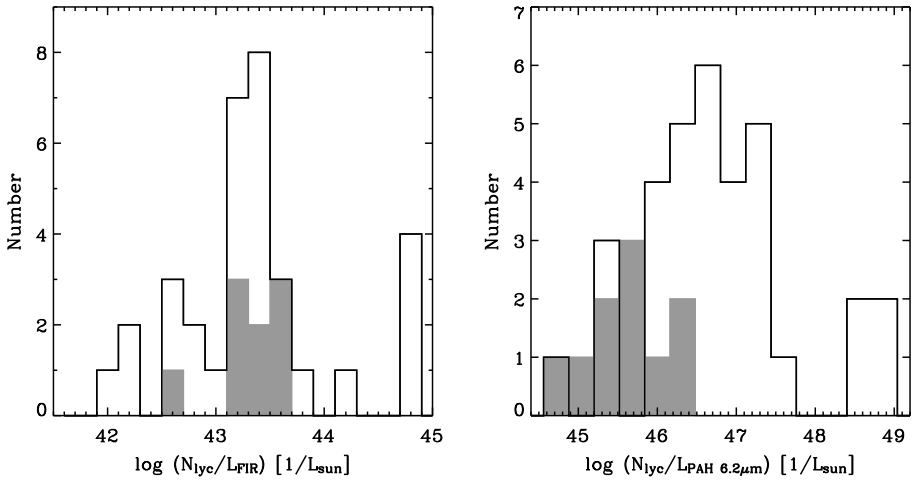

FIGURE 7.16 — The different distributions in N_{lyc}/L_{FIR} **(left panel)** and $N_{lyc}/L_{6.2PAH}$ **(right panel)** for the Galactic and LMC H II regions (*solid line*) and the starburst galaxies (*grey scale*). The highest value for both ratios corresponds to the 4 positions within 30 Dor.

therein). PAHs may also provide a convenient tracer of star formation activity as the discussion on the starburst and ULIRGs in this paper exemplifies. PAHs are stochastically heated by UV photons produced by massive stars. Assuming fixed emission and absorption properties and fixed PAH abundance, the PAH emission is a measure of the amount of photons available between 6 and 13.6 eV (the former corresponding with the averaged ionisation potential of PAHs) and hence of star formation. To assess the robustness of this new tracer, we compared it to two tracers, N_{lyc} and L_{FIR}, for both Galactic star forming regions and galaxies (normal and starbursts).

L_{FIR} is a tracer for star formation since a significant fraction of the stellar radiation is emitted by (young) stars with spectral types mid-B or earlier. Much of this radiation is absorbed by dust and re-emitted thermally in the FIR. The number of ionizing photons, N_{lyc}, is commonly used as a measure of massive star formation. It is mainly derived in three ways, 1) from the Hα recombination line; 2) from radio recombination lines and 3) from the hydrogen free-free continuum emission at radio wavelengths. For the Galactic and LMC H II regions, N_{lyc} is obtained from radio continuum emission (Martín-Hernández et al. 2002; Martín-Hernández et al. 2003; Vermeij et al. 2002). For galaxies, on the other hand, free-free radio emission may be confused by non-thermal synchrotron emission from young SNR or AGNs. Their N_{lyc} is therefore obtained from near- and mid-infrared hydrogen recombination lines (Genzel et al. 1998; Verma et al. 2003; Förster Schreiber et al. 2001).

The three tracers are compared with each other in Fig. 7.15. L_{FIR} is in first order clearly proportional to $L_{6.2PAH}$. However, their ratio is significant different between the Galactic H II regions ($5.5\pm4.6\ \ 10^{-4}$) and the galaxies ($6.3\pm3.2\ \ 10^{-3}$), with Orion and the reflection nebulae having a similar and lower ratio as the galaxies, respectively (also seen in Figs. 7.4 through 7.9). In contrast, this discrepancy between the Galactic and extragalactic sample is not present in the L_{FIR}/N_{lyc} ratio, though a slightly larger scatter is observed in each of these

groups. In addition, $L_{6.2PAH}$ is roughly proportional to N_{lyc} for the galaxies while for the Galactic H II regions, it is much less dependent on N_{lyc}. In fact, the $L_{6.2PAH}$ observed in H II regions, seems to be almost independent of the hardness of the radiation field.

As discussed by e.g. Kennicutt (1998), and references therein, the efficiency of L_{FIR} as a tracer for star formation depends on the type of galaxies considered, being highest for dusty circumnuclear starbursts. Indeed, the FIR spectra of galaxies are composed of emission of dust around young star-forming regions and emission of more extended dust heated by the interstellar radiation field. The same holds for PAHs as a tracer of star formation. Likewise, the observed PAH flux is integrated over the whole galaxy and therefore includes PAH emission originating in the ISM, reflection nebulae, exposed PDRs and embedded compact H II regions. This ISM contribution can be estimated by comparing $L_{6.2PAH}$ with N_{lyc} (since it does not suffer from this contamination) for both the H II regions — as a template for massive star formation — and the galaxies. Concerning L_{FIR}, the galaxies show a similar distribution of N_{lyc}/L_{FIR} as the H II regions (Fig. 7.16) and so L_{FIR} is likely not influenced by an ISM contribution in these galaxies. In contrast, the galaxies have a clearly different distribution in $N_{lyc}/L_{6.2PAH}$, with — on average — a lower ratio, indicating that the PAH emission in galaxies partly originates in the ISM. Therefore, PAHs may be better suited as a tracer of B stars, which dominate the Galactic stellar energy budget, than as a tracer of massive star formation.

7.5.3 Conversion from PAH luminosity to IR luminosity

Recently, Soifer et al. (2002) and Lutz et al. (2003) have used PAH emission features as a quantitative measure for the contribution of exposed star formation to the bolometric luminosity of two ULIRGs (Arp 220 and NGC 6240). While Soifer et al. (2002) assumed the ratio of L(11.2PAH) and L(IR) for the starburst core in M 82 to be a measure for exposed star formation, Lutz et al. (2003) instead used the mean L(7.7PAH)/L(IR) ratio derived from a sample of 10 starburst nuclei. A third method to derive the bolometric correction was proposed in Chapter 6 and is based on the mean L(6.2PAH)/L(IR) ratio for our sample of normal and starburst nuclei. This ratio is 0.0034 ± 0.0017.

For sources where the environment of massive star formation resembles exposed PDRs (such as M 82 and NGC 253; Carral et al. 1994; Lord et al. 1996), the three methods discussed above will give reasonable results. On the other hand, for sources which resemble embedded star formation (e.g. Arp 220 and NGC 4418), a ten times lower ratio, appropriate for compact H II regions like W3, might be a better choice. This issue cannot be decided based upon the mid-IR spectra alone. Observations of PDR lines such as the [O I] 63 μm and [C II] 158 μm lines can be very instrumental in resolving this issue. In that respect, we note that the PDR fine structure lines are very weak in Arp 220 (Luhman et al. 2003), suggesting also that the PDR component is underdeveloped, perhaps due to absorption of a major fraction of the FUV flux by dust inside the H II region (Luhman et al. 2003).

7.6 Conclusions

In this Chapter, the MIR spectral chararcteristics of Galactic and extragalactic soures are investigated. Our sample includes Galactic (C)H II regions, ISM lines of sight and embedded massive protostars as well as normal galaxies, starburst galaxies, Seyferts, QSOs and (ultra-luminous) infrared galaxies.

First, the MIR spectrum of each object type is described and compared, revealing distinct spectral characteristics for each object type. In order to distinguish the different natures of the galaxies, i.e. AGN-dominated, starburst-dominated or heavily obscured, we then present a new MIR/FIR diagnostic based on the ratio of the 6.2 PAH emission band to FIR flux and the ratio of the 6.2 μm continuum to FIR flux. This study has demonstrated that the 6.2PAH/6.2cont ratio is remarkably constant over a wide range of Galactic H II regions, as well as more general ISM material. As such, it provides a very clear handle on any AGN contribution to the MIR. Indeed, AGNs are found to seggregate in two groups; most type-2 Seyferts are located with the normal and starburst galaxies, while most type-1 Seyferts show strong 6.2cont/FIR ratios. The 6.2 μm PAH luminosity distributions are found to be independent of the Seyfert type, in accordance with the orientation dependent AGN unification scheme, and hence confirm the results of Clavel et al. (2000). This diagram further reveals the spectral resemblance of starburst and normal galaxies to exposed PDRs rather than embedded compact H II regions. ULIRGs show a diverse spectral appearance. Some show a typical AGN hot dust continuum. More, however, are either starburst-like or show signs of strong dust obscuration in the nucleus. One characteristic of the ULIRGs seems also to be the presence of more prominent FIR emission than either starburst galaxies or AGNs. Comparison with the diagnostic diagrams proposed by Genzel et al. (1998) and Laurent et al. (2000) for our sample indicates that the ability to identify obscured objects is best achieved with our MIR/FIR diagnostic, while the ability to identify the presence of an optically-recognized AGN is best achieved with the Genzel diagram.

We found that the observed variation of the MIR/FIR diagnostic ratios in the Galactic sample is linked with their evolutionary state and the PAH/dust abundance. Finally, we have examined the use of PAHs as quantitative tracers of star formation activity and find that PAHs may be better suited as a tracer of B stars, which dominate the Galactic stellar energy budget, than as a tracer of massive star formation. Hence, the PAH emission of normal and starburst galaxies is best represented by that of exposed PDRs such as the Orion Nebula. However, the infrared spectra of some sources — notably the architypal ULIRG Arp 220 — may be dominated by embedded massive star formation rather than exposed PDRs. NGC 4418 may be an even more extreme example of such buried star formation, where even the faintest traces of PAH are lacking.

Acknowledgements

The authors are gratefull to W. Reach for providing the ISO–CAM–CVF data of the SMC molecular cloud, S. Madden for providing ISO–CAM–CVF galaxy spectra prior to publication and J.P. Simpson for providing the MSX Orion spectrum. This research has made use of the NASA/IPAC Extragalactic Database (NED) which is operated by the Jet Propulsion Laboratory, California Institute of Technology, under contract with the National Aeronautics and Space Administration.